



OPEN

Fabrication of N-doping activated carbons from fish waste and sawdust for Acid Yellow 36 dye removal from an aquatic environment

Mohamed A. El-Nemr¹✉, Mohamed A. Hassaan² & Ibrahim Ashour¹

Acid Yellow 36 (AY36) dye is a synthetic azo dye that is excessively used in various industries, causing hazardous environmental effects. The main target of this study is the preparation of self-N-doped porous activated carbon (NDAC) and the investigation in eliminating the AY36 dye from the water solution. The NDAC was prepared by mixing fish waste (60% protein content) which was considered a self-nitrogen dopant. A combination of Fish waste, sawdust, zinc chloride and urea with a mass ratio (5:5:5:1) was submitted to hydrothermal process at 180 °C for 5 h followed by pyrolysis for 1 h under N₂ stream at 600, 700, and 800 °C. Fabricated NDAC was qualified as an adsorbent for recovering AY36 dye from water using batch trials. The fabricated NDAC samples were characterized by FTIR, TGA, DTA, BET, BJH, MP, *t*-plot, SEM, EDX, and XRD methods. The results showed the successful formation of NDAC with nitrogen mass percentage content (4.21, 8.13 and 9.85%). The NDAC prepared at 800 °C had the largest nitrogen content (9.85%) and was labeled as NDAC800. This later had 727.34 m²/g, 167.11 cm³/g, and 1.97 nm for specific surface area, the monolayer volume and the mean pores diameter respectively. By being the more efficient adsorbent, NDAC800 was chosen to test AY36 dye removal. Therefore, it is selected to investigate the removal of AY36 dye from aqueous solution by varying important parameters such as solution pH, initial dye concentration, adsorbent dosage and contact time. The removal of AY36 dye by NDAC800 was pH-dependent, with the optimum pH value 1.5 giving 85.86% removal efficiency and 232.56 mg/g maximum adsorption capacity (*Q_m*). The kinetic data exhibited the best fit model with the pseudo-second-order (PSOM), while the equilibrium data fit well with the Langmuir (LIM) and Temkin (TIM). The mechanism of AY36 dye adsorption may be ascribed to the electrostatic contact between the dye and the available charged sites on NDAC800 surface. The prepared NDAC800 may be considered as an efficient, available, and eco-friendly adsorbent for AY36 dye adsorption from simulated water.

Nowadays, the insufficiency of clean and fresh water resources becomes the biggest obstacle in order to meeting the progress of the civilization of humanity. Persistent pollution is considered a major factor that threatens the world's water resources. Many attempts have been made to create solutions to compensate the shortage of various water resources, but these attempts are still quite limited. So, it became necessary to link scientific research with all types of water treatment.

One of the most toxic pollutants is organic dyes which are harmful to living things and the environment. Acid Yellow 36 dye is a mono azo dye, water-soluble, pH indicator and has various applications such as leather, paper and textile industries^{1–4}. Many treatment procedures are utilized for water treatment, depending on the type of treated objectives⁵. Generally, methods for water treatment processes are adsorption⁶, oxidation procedures (photocatalysis)^{7–9}, precipitation¹⁰, coagulation/flocculation¹¹, reverse osmosis¹², ion exchange¹³, filtration¹³, biological treatment¹⁴ and advanced oxidation processes^{15–19}. Adsorption technique is the most effective water purification process due to its simplicity, effectiveness and eco-friendly advantage of the absence of generated

¹Department of Chemical Engineering, Faculty of Engineering, Minia University, Minia 61519, Egypt. ²Environment Division, National Institute of Oceanography and Fisheries (NIOF), Kayet Bey, El-Anfoushy, Alexandria, Egypt. ✉email: mohamedelnemr1992@yahoo.com

sludge^{20–24}. Adsorption method owned many advantages such, as its low cost, appropriateness and effortlessness of process and designs^{25,26}, ease of use, low energy requirements, and lack of production of harmful side effects from conventional treatments¹¹. Due to their accessibility, ease of preparation, and exceptional adsorption capacity findings, activated biomass-based treatments are thought to have received recently more attention among the numerous available adsorbents for dyes removal from liquid effluents^{25–27}.

Especially, various technological systems for removing dyes were examined such as the photocatalytic degradation using ZnO as a photocatalyst²⁸, reverse micelles²⁹, Photoelectro-Fenton using iron electrodes³⁰, adsorption onto green nano-ceria, and NH₂ functionalized green nanoceria³¹, Orange peels, and Rice Husk³², and Pinecone³³, solvent extraction using the carrier trioctylamine³⁴ and electrocoagulation using iron electrodes³⁵.

One of the best methods for improving activated carbon's adsorption effectiveness is nitrogen doping, which increases its electronic conductivity, adds additional ion-storage sites, and reduces amplitude because the nitrogen atom has one more electron than the carbon atom^{20–23,36}. The doped nitrogen atoms within the six-membered carbon ring create local stress when it is added to a carbon material, which causes the deformation of the original carbon structure³⁷.

The lone pair of electrons that nitrogen atoms carry would delocalize the initial sp² hybrid electron cloud on the carbon skeleton, improving electron transportation and reactivity of the activated carbon surface since nitrogen atoms have a higher electronegativity (3.04) than carbon atoms (2.55). Simultaneously, doped nitrogen atoms can significantly enhance carbon compound adsorption by giving additional free electrons²³. Recent studies showed that doping-activated carbons with a specified amount of nitrogen, sulphur, or phosphorus enhance their surface stability as well as a portion of their pseudo capacitance, boosting their overall specific capacity^{38–40}. Surface groups on activated carbons have a significant role in defining the electrochemical interface state as well as the properties of carbon surfaces. These qualities include stability, isoelectric point, contact resistance, ion adsorption, and self-discharge, among others⁴¹. The existence of efficient heteroatom groups on the surface of activated carbons is expected to enhance their ion adsorption capacity as well as their hydrophilicity/lipophilicity. As a result, it is believed that modifying the surface properties of carbon materials is good policy to boost efficiently the adsorption capacity of carbon-based materials. Nitrogen doping in carbon matrices can take several forms. There are two types of doping: post-treatment doping (PTD) and in-situ doping (ISD) as reported in the literature³⁷. Chemical vapor deposition (CVD), solvent-thermal synthesis, and laser ablation are examples of ISD processes. PTD procedures include plasma therapy, irradiation, and thermal annealing at high temperatures. A more advanced and less-doped method than post-treatment doping is the ISD of nitrogen-rich precursors. Therefore, there has been a lot of interest in producing of high nitrogen-doped activated carbons (NDACs) following PTD way⁴². NDACs have been widely used in numerous fields to improve their characteristics and mobility by nitrogen-doping activated carbon. Recently, nitrogen-doped carbon compounds have been identified as potential materials for heterogeneous catalysis, such as catalytic hydro-de oxygenation, which is a key step in refining bio-oil before creating high-value chemicals or transportation fuels⁴³. Nitrogen doping protects the pores structure of carbon materials and improves their electrochemical characteristics, making them suitable for use as supercapacitors^{44–47}. Additionally, the metal contained within a nitrogen-doped carbon nanosphere was used as a photocatalyst, opening new avenues for environmental pollution remediation. In general, photocatalysis using solar energy is viable for addressing energy shortages and pollution⁴⁸. With a large specific surface area, NDACs could be excellent materials for removing contaminants such as toxic pollutants from wastewater²⁴. Furthermore, NDACs can be used as an electro-catalyst in manufacturing⁴⁹. Similarly, activated carbon doped with nitrogen can be employed as a novel material with a high CO₂ collection capacity⁵⁰.

El-Nemr et al.²¹ developed modified biochars from pea *Pisum sativum* using NH₂ and TETA and assessed its use for enhancing the adsorption capacity of Acid Orange 7 (AO7) dye. The removal of AO7 dye using the modified (PeaNH₂ and Pea- TETA) biochars derived from the pea *Pisum sativum* peels were investigated. The adsorption capacity at equilibrium (q_e) of the modified biochar was significantly enhanced from 78.18 for unmodified biochar to 523.12 mg/g for Pea- TETA biochar at initial concentration 300 mg/L and dosage 0.50 g/L. The percentage removal of AO7 dye reached 99% for Pea- NH₂ and 98% for Pea-TETA. Sun et al.⁴⁹ fabricated nitrogen self-doped porous activation carbon (N-PAC) with large specific surface area (SBET = 1300.58 m²/g) as bifunctional electrocatalysts. The N-PAC is prepared by a simplistic pyrolysis process from marine algae at controlled temperature with ZnCl₂.

Thirunavukkarasu et al.³¹ use the green nanoceria synthesized from *Prosopis juliflora* (Sw.) leaves extract, which amine functionalized to GN-NH₂ (AGN) with epichlorohydrin and ammonium hydroxide. In the ambient temperature and at acidic pH of 2, the maximum removal efficiency of AY36 is 92.9% for AGN respectively. The kinetic data exhibited good correlation coefficient (r² > 0.99) for the pseudo-second-order and elovich models with marginal error values signifying the chemisorption type of adsorption process. The maximum adsorption capacities of AGN was 26.95 (mg/g).

The main goal of this paper is to focus on and describe a novel technique for the fabrication of nitrogen self-doping activated carbon (NDAC) with a high nitrogen content at different temperature with ZnCl₂ as (activation reagent) and investigate its effects on the removal of AY36 dye from water.

Materials and methods

Chemicals and equipments. Ethanol (C₂H₅OH), urea (NH₂CONH₂), Zinc chloride (ZnCl₂), and Acid Yellow 36 dye (AY36) (Molecular formula: C₁₈H₁₆N₃NaO₃S; Molar Mass: 377.39 g/mol; λ_{max}: 450 nm) were obtained from Sigma Aldrich, USA. Sawdust was obtained from a local carpenter, Alexandria, Egypt. Fish waste (mixture of *Atherina hepsetus* and *Sardina Pilchardus* Fishes waste of 60% protein) was obtained from the NIOF, Egypt. HCl, (30–34%) was obtained from (SD-FCL), Mumbai, India. UV-visible spectrophotometer (Analytic Jena, model SPEKOL1300) has glass cells of 10 mm optical path used for dye concentration determination.

Shaker (A JS shaker, model JSOS-500), Thermo shaker incubator (GSSI-100T sh), Nabertherm B180 Tubular Furnace (RT 50/250/13), and pH meter JENCO (6173) were used for the experimental work. Fourier transform infrared spectrometer (FT-IR: Bruker Vertex 70 connected to Platinum ATR model V-100). X-ray Photoelectron Spectroscopy (XPS) was performed using a Thermo Fisher Scientific K-Alpha XPS with a pass energy of 50 eV at a base pressure of ~10^{−9} mbar.

The BET surface area (S_{BET}) studies of the NDACs were done using N₂ adsorption–desorption analysis at 77 K using an analyzer instrument (BELSORP—Mini II, BEL Japan, Inc.) The BET^{51–53}, analysis of the adsorption–desorption isotherm curve was used to calculate the monolayer volume (V_m) (cm³ (STP)/g), the specific surface area (S_{BET}) (m²/g), the volume of the total pore (V_T) (p/p₀) (cm³/g), mean pore diameter (nm) and energy constant (C). The following equation was used to determine the average pore-radius (1):

$$r(\text{nm}) = \frac{2V_T(\text{mLg}^{-1})}{a_{s,\text{BET}}(\text{m}^2\text{g}^{-1})} \times 1000 \quad (1)$$

Using the Barrett-Joyner-Halenda (BJH) methodology, the BELSORP analysis programme software was also used to calculate the micropore surface area (S_{mi}) and micropore volume (V_{mi}), as well as the mesopore surface area (S_{mes}) and mesopore volume (V_{mes}), of biochar. The pore size distribution (PSD) was calculated using the BJH approach from the isotherm desorption curve⁵⁴.

Thermal-gravimetric analyses (TGA) were performed using the SDT650 instrument in a temperature range of 25–1000 °C, at 10 °C per minute, as a temperature ramp under 100 mL/min flow of nitrogen gas⁵⁵. Scanning Electron Microscope (SEM) examination was carried out utilizing a Quanta 250 FEG SEM instrument with 500 kV HV, and large-field low vacuum SED (LED) coupled with EDX unit to analyze the surface-morphology and porosity of the NDACs. D2 PHASER Instrument, manufactured by Bruker in Germany, was used for the XRD analysis.

Preparation of self-Nitrogen doped activated carbon (NDAC). The NDACs were prepared by a uniform mixing of sawdust with ZnCl₂, Fish waste (60% protein) and urea in a mass ratio of 5:5:5:1 and distilled water (300 mL). The prepared mixture was transported to a 500 mL Teflon cup (1,1,2,2-polytetrafluoroethylene) and treated hydrothermally by placing it into a stainless steel autoclave at 180 °C for 5 h. This prepared fusion material was then dried at 125 °C for 24 h. The carbonization of the dried mixture to form NDACs was performed via pyrolysis in the high-temperature area of the tubular furnace under N₂ stream rate of 100 mL/min. The pyrolysis process was realized at 600, 700 and 800 °C and kept constant at this temperature for 1 h. The obtained NDACs were refluxed in 2N HCl solution for 2 h, filtered, washed with EtOH followed by distilled water and oven dried overnight at 125 °C. Finally, the targeted NDACs were labeled as NDAC600, NDAC700, and NDAC800 (Fig. 1S).

pH of point of zero charge (pH_{PZC}). The approach outlined in the literature was used to obtain the pH_{PZC}^{56,57}. In brief, in 100 mL flasks, 50 mg of NDAC800 was taken in 50 mL of 0.1 M NaNO₃ solutions. The initial pH solution (pH_i) was adjusted to a value ranged from 2 to 12 using 0.1 M HCl or NaOH and shaken 24 h. Then the final pH of the supernatant liquid (pH_f) was calculated. Moreover, the variance at the beginning and final pHs ($\Delta\text{pH} = \text{pH}_i - \text{pH}_f$) was plotted against the pH_i. The pH value at the ΔpH equalled zero was ascribed as pH_{PZC} of the adsorbent. The pH_{ZPC} value of NDAC800 was reported to be 8.85 (Fig. 1). The result designates that, below this pH value, the surface of the NDAC800 has a positive charge due to the protonation of nitrogen atoms into NDAC-H⁺.

Acid Yellow 36 dye adsorption. 1.0 g/L stock solution of AY36 dye was prepared by dissolving 1.0 g of AY36 dye into 1 L distilled water. The removal investigation of AY36 dye was carried out using the batch equilibrium technique. In a shaker, 100 mL of AY36 dye solutions of various concentrations were agitated with various amount (50 to 250 mg) of the produced NDAC. The solution was examined using a UV–visible spec-

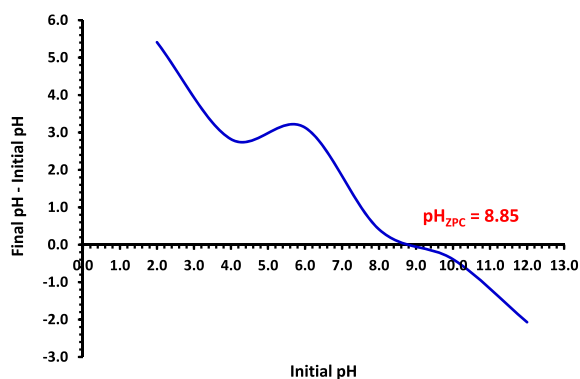


Figure 1. The pH_{ZPC} determination of the NDAC800 at 25 ± 2 °C.

trophotometer at $\lambda = 450$ nm for AY36 dye residual concentration determination. The adsorption capacities of nitrogen-doped activated carbon can be measured using Eq. (2):

$$q_t = \frac{(C_0 - C_t)}{w} \times V \quad (2)$$

where q_t (mg/g), C_0 (mg/L), and C_t (mg/L) are the capacity of adsorbent at time t , the initial concentration of dye; the residual concentration of the pollutant after adsorption had taken place over a period time t , respectively. V (L) and W (g) are the waste solution volume of dye in liters and the mass of NDAC in grams. The following equation is applied to measure the AY36 dye elimination % from the water solution (3):

$$\text{Removal}(\%) = \frac{(C_0 - C_t)}{C_0} \times 100 \quad (3)$$

The impact of pH on AY36 dye removal was studied using 100 mg of NDAC800 and 100 mL of AY36 dye solutions (100 mg/L) by varying the initial pH values 1.5, 3, 5, 7, 9 and 11. The solution pH was adjusted using HCl (0.1 M) or NaOH (0.1 M) solutions. The mixtures were agitated at 200 rpm for 2 h at 25 ± 2 °C and the final AY36 dye was determined.

The impact of adsorbent dose and the isotherm study were performed using different concentrations of AY36 dye solutions (100–400 mg/L) using various weights of NDAC800 (50–250 mg) in 100 mL of AY36 dye solutions. Then the solutions were shaken at 200 rpm for 10, 15, 30, 45, 60, 90 and 120 min at 25 °C and the supernatants were analyzed spectrophotometrically.

Results and discussion

Morphology and structure description. *FTIR analysis.* The efficient groups of raw sawdust, fish waste, the mixture (sawdust, fish waste, ZnCl_2 and urea) and NDAC800 were determined by FTIR and shown in Fig. 2a–e. The FTIR spectrum of sawdust (Fig. 2a) shows the appearance of an absorption broad peak at 3334.66/cm, proving the occurrence of free and intermolecular bonded –OH groups. The appearance of the peak at 2899/cm assigned to C–H stretching vibrations from – CH_2 group, and the peak at 1723.59/cm corresponds to –C=O stretching vibrations from aromatic groups of lignin. The appearance of a peak at 1634.45/cm may be due to N–H amide group, and the peak at 1422.97/cm is due to –OH deformation. Another strong sharp peak at 1026.04/cm characterizes C–O stretching of the primary alcohol. At last, the peaks at 590.43 and 557.99/cm were related to the bending vibration modes of aromatic compounds (Fig. 2a). The FTIR spectrum of the fish waste (mixture of *Atherina hepsetus* and *Sardina Pilchardus*) is represented in Fig. 2b, which showed for amide A, two broad bands, one of them appeared at 3279.36/cm is due to OH while the other broad peak at 3066.73/cm is attributed to N–H stretching vibrations. The occurrence of two broad bands of amide B at 2924.18 and 2852.78/cm correspond to CH_2 stretching vibrations. The peak of ester and lipids groups is observed at 1738.06/cm. Also, amide I, II, and III have appeared at 1627.3 (stretching vibration of C=O), 1541 (N–H bending and C–N stretching vibrations), 1308 and 1232.55/cm (N–H bending and C–N stretching vibrations and O=C–N), respectively. Finally, absorption peaks at about 1104.31, 1040.41, 603.61 and 533.73/cm assigned to asymmetric stretching of phosphate group (PO_4^{3-}). The FTIR of pure urea is shown in Fig. 2c. The N–H stretching peak appeared at 3428.85–3255.57/cm, and the C=O stretching peak appeared at 1669/cm. The N–H deformation stretching peak appeared at 1586.35/cm, while the C–N stretching peak appeared at 1457/cm. The FTIR of the mixture of raw sawdust, fish waste, ZnCl_2 and urea was shown in Fig. 2d. The peak of O–H stretching for alcohol and the N–H stretching frequencies had become stronger, broader, and appeared at 3337.00 and 3218.61/cm, respectively. Occurrence of two broad bands at 2924.43 and 2855.47/cm are due to CH_2 stretching vibrations of sawdust and amide B. The appearance of strong sharp wide peak at 1604.04/cm which representing the N–H amide group in sawdust, amid I in fish meal and in urea. The appearance of N–H bending and C–N stretching vibrations of amide II at 1507.46, while the C–N stretching peak in urea appears at 1414.21/cm. The FTIR analysis of NDAC800 was given in Fig. 2e. The broad set of peaks with low intensity appeared between 3745 and 3096.68/cm are corresponding to N–H stretching. The appearance of these peaks may be due to the hydrogenation of some of the nitrogen atoms. The C–H stretching has a broad low-intensity peaks appeared at 2897.11 and 2808.46/cm. The appearance of low-intensity peaks at 2394.36, 2348.46, and 2322.76/cm are assigned to $\text{C}\equiv\text{N}$ stretching vibrations of isonitrile-cyano-terminal groups. The allene ($\text{C}=\text{C}=\text{C}$) and ketamine ($\text{C}=\text{C}=\text{N}$) groups appeared as a set of medium peaks at 2229.50–2048.54/cm. The band owing to C=C stretching vibration is performed at 1705/cm. The appearance of the strong sharp peaks, which relevant to sp^2 structure of the carbon atoms with a higher shifting from 1508.57 to 1577.72/cm and from 1026.09 to 1107.12 and 1053.22/cm confirmed the successful formation of nitrogen doping activated carbon at 800 °C. This shifting may occur due to nitrogen doping which causes the disordered structure of the carbon network.

BET analysis. The N_2 adsorption–desorption isotherms of NDAC600, NDAC700 and NDAC800 are represented in Fig. 3a–f. These concluded that the adsorption isotherm of the various nitrogen NDACs are microporous typical type I and subsequently possessed a strong interaction between NDAC surface and adsorbate (Fig. 3a). According to BET analysis results (Table 1, Fig. 3b), NDAC600 has a surface area, monolayer volume, total pore volume, and mean pore diameter of 553.63 m^2/g , 127.20, 0.2844 m^3/g and 2.0584 nm, respectively while NDAC700 possessed the highest surface area of 783.78 m^2/g , monolayer volume, mean pore diameter, and total pore volume of 180.08 cm^3/g , 2.0194 nm, and 0.3957 cm^3/g , respectively. The specific surface area of NDAC800 was 727.34 m^2/g , the monolayer volume, total pore volume, and mean pore diameter were 167.11, 0.3576 cm^3/g and 1.9668 nm, respectively. Observably, the mean pore diameter value of NDAC800 is margin-

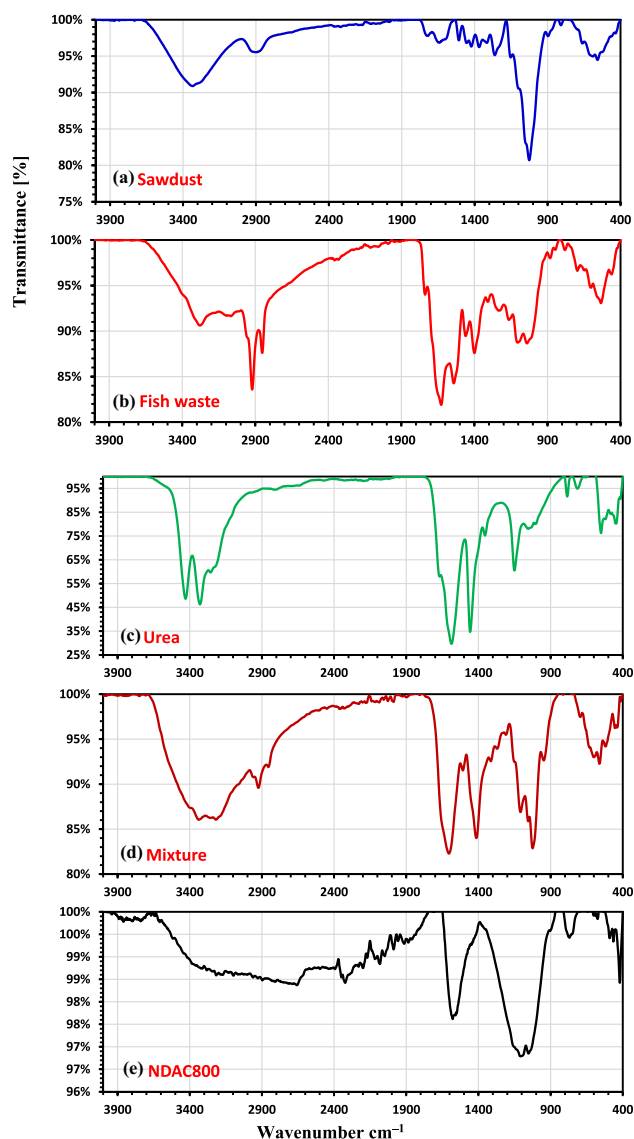


Figure 2. The FTIR studies of (a) raw sawdust; (b) raw fish waste materials of 60% protein; (c) urea; (d) the mixture (raw sawdust, fish waste, ZnCl_2 and urea) hydrothermal; and (e) NDAC800.

ally decreased than the other NDAC at 600 and 700 °C, indicating that the increase in temperatures from 600 to 800 °C may be slightly affected on the formation of micropore of NDAC800. The t -plot analysis reflected the correlation between the thickness of adsorption layer and relative pressure. The t -plot curves of NDAC600, NDAC700, and NDAC800 are shown in Fig. 3c. t -plot analysis of NDAC at 600, 700, and 800 °C showed type II, which meant that they possessed uniformly sized micropores. From Table 1, the pore surface area of NDAC prepared at 600, 700 and 800 °C are 640.649, 894.315 and 864.640 m^2/g , respectively. The pore volume of NDAC at 600, 700 and 800 °C were 0.2441, 0.3515 and 0.3193 cm^3/g , respectively, while the average pore diameter are 0.7573, 0.7813 and 0.7341 nm, respectively. The MP-conclusions plot's are quite similar to those of a t -plot because it is an analysis technique derived from one. The MP-plot is significantly impacted by the chemical differences between standard material and sample surface, as well as by the action of micropore filling, hence it cannot create a smooth curve. However, the MP-plot can be used to determine whether micropores exist and what size range they fall into. The MP-plot of NDAC at 600, 700 and 800 °C are shown in Fig. 3d, which shows that NDAC prepared at 600, 700, and 800 °C has micropores of 0.3–1.1 nm diameter, a maximum distribution peak at 0.5 nm while the distribution area of pores in NDAC800 is the largest one. Also, the surface area and the volume of pores were shown in Table 1. The pore surface area (a_1 – a_2) of NDAC600, NDAC700 and NDAC800 was 604.981, 851.67 and 810.177 m^2/g while the pore volume (V_p) was 0.2536, 0.3626 and 0.3337 cm^3/g , respectively. BJH analysis desorption and adsorption used to determine the distribution of the mesopores pore size. BJH analysis desorption–adsorption of NDAC at 600, 700 and 800 °C are shown in Fig. 3e, f and Table 1. From Fig. 3e, the NDAC600 has a 2.3–9.0 nm radius of mesopore, and it has a distribution peak at 3.0 nm. The NDAC700 has 2.5–10.0 nm radius of mesopores, and it has a distribution peak at 3.5 nm, while

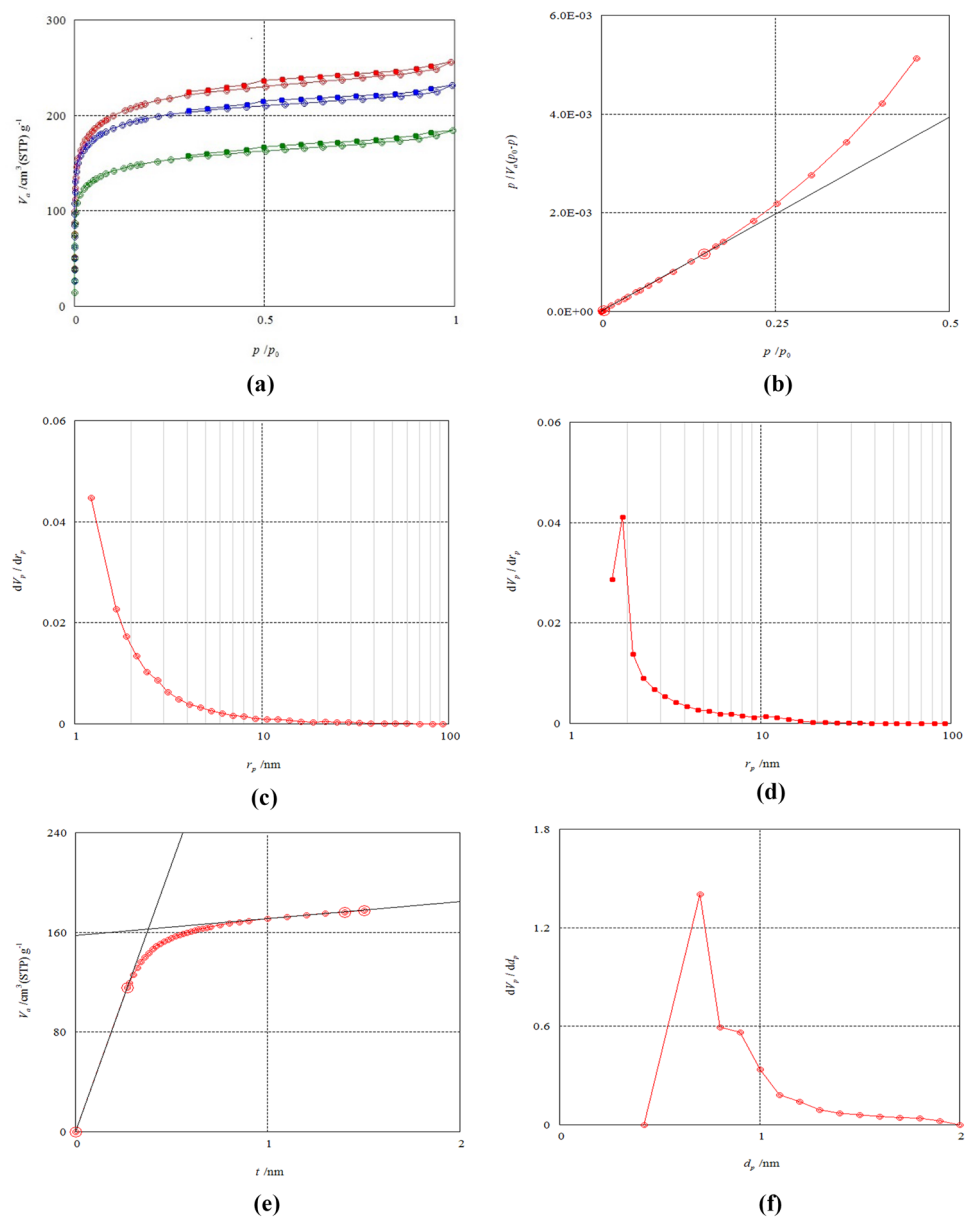


Figure 3. (a) Adsorption–desorption of NDAC600 (green), NDAC700 (red) and NDAC800 (blue); (b) BET analysis of NDAC800; (c) BJH analysis by adsorption of NDAC800; (d) BJH analysis by desorption of NDAC800; (e) t -plot analysis of NDAC800; (f) MP analysis of NDAC800.

the NDAC800 has 2.2–9.0 nm radius of mesopores, and it has a distribution peak at 3.1 nm (Fig. 3e). The BJH desorption analysis of NDAC600, NDAC700, and NDAC800 had integrated pore volume (V_p) 0.0512, 0.0609 and 0.0499 cm^3/g , and the mesopore specific surface area 32.867, 40.589 and 32.378 m^2/g , respectively (Table 1). The BJH adsorption analysis of NDAC600, NDAC700 and NDAC800 had integrated pore volume (V_p) 0.0822, 0.1090 and 0.0862 cm^3/g and the mesopore-specific surface area 76.743, 109.490 and 84.850 m^2/g , respectively (Table 1). Generally, from the BJH desorption and adsorption results showed the mesopore specific surface area represented a marginal amount of the total specific surface of nitrogen doping activated carbons. The increase in temperature from 600 to 700 °C showed an increase in surface area, while a further increase in temperature from 700 to 800 °C resulted in a slight decrease in surface area, which may be attributed to the deformation of the structure of the prepared activated carbon.

EDX analysis. About 60% of fish waste is a protein mainly containing C, N, O, H elements, and it is hydrolyzed at high temperatures. The process of preparing of self nitrogen-doped porous activated carbons (NDACs) by hydrothermal at 180 °C and then pyrolysis under nitrogen gas flow at high temperatures (600, 700, and 800 °C) is actually the removing method of non-carbon elements and carbon skeleton rearrangement with introducing of the nitrogen atom in the carbon network. Zinc chloride was used as an impregnation reagent to improve the

Analysis method	Sample entry		NDAC600	NDAC700	NDAC800
	AC yield	(%)	25.03	25.757	21.545
BET	$a_{s, BET}$ (m ² /g)	S_{BET} (m ² /g)	553.63	783.78	727.34
	V_m (cm ³ /g)	V_m (cm ³ (STP)/g)	124.2	180.08	167.11
	Mean pore diameter	D_p (nm)	2.0584	2.0194	1.9668
	Volume of total pore	V_T (cm ³ /g)	0.2849	0.3957	0.3576
t-plot	a_1 - a_2	S_{mi} (m ² /g)	640.649	894.315	864.64
	V2	V_{mi} (cm ³ /g)	0.2441	0.3515	0.3193
	2t	(nm)	0.7573	0.7813	0.7341
MP	a_1 - a_2	(m ² /g)	604.981	851.67	810.177
	V_p	(cm ³ /g)	0.2536	0.3626	0.3337
BJH ads	V_p	(cm ³ /g)	0.0822	0.109	0.0862
	a_p	(m ² /g)	76.743	109.49	84.85
BJH des	V_p	V_{me} (cm ³ /g)	0.0512	0.0609	0.0499
	a_p	S_{me} (m ² /g)	32.867	40.58	32.378

Table 1. Analysis of the surface area of fabricated Nitrogen-doping activated carbons.

pores formed during the pyrolysis process⁵⁸. At higher temperatures, ZnCl₂ will evaporate as a gas to form pores. ZnCl₂ combines with oxygen in OH functional groups to cause a dehydrogenation and dehydration process of the hydroaromatic structure. Therefore, the NDAC600, NDAC700 and NDAC800, have higher carbon content but a relatively low oxygen as shown in Table 2. According to EDX analysis of NDAC600 possessed 74.19% of carbon, a high amount of nitrogen that was 8.13%, 11.18% oxygen, low amounts of silicon and sulphur, which were 0.94 and 0.86%, respectively, 3.79% chlorine and 0.9% zinc. The EDX analysis of NDAC700 consisted of 81.38% carbon, 4.21% nitrogen, 8.41% oxygen, low amounts of silicon and sulphur, which were 0.52 and 0.72%, respectively, 3.75% chlorine and 1.01% zinc. While the EDX analysis of NDAC800 consisted of 76.73% carbon, 9.85% nitrogen, 8.97% oxygen, low amounts of silicon and sulphur, which were 0.60 and 0.43%, respectively, 2.70% chlorine and 0.73% zinc (Table 2, Fig. 4a–c). From these results it can deduced that the NDAC800 has the highest nitrogen content.

Scanning electron microscope (SEM). Figure 5a–d displayed the SEM pictures of raw sawdust, NDAC800, NDAC700 and NDAC600, respectively. From Fig. 5a, the raw sawdust appears as a heterogeneous macroscopic smooth surface with large numbers of crumples and lappets. Also, Fig. 5b shows that the nitrogen-doped activated carbon prepared at 800 °C has obvious channel-pores with an abundant uniform distribution of channel-pores size. The average size of all micropores is < 2 nm as proved by BET analysis of the samples (Table 1). This result proved that the N-atoms were successfully introduced into the skeleton structure of activated carbons with the highest microporosity. Figure 5c and d represent the SEM images of NDAC700 and NDAC600, respectively.

X-Ray diffraction (XRD) study. XRD analysis of the fabricated NDAC600, NDAC700 and NDAC800 were presented in Fig. 6. The XRD spectra of all nitrogen-doped activated carbons reflect two peaks around 24° and 44° assigned to the (002) and (101) plans of carbons, respectively. In this case, the weak intensity peak would reveal the smaller crystallites, which is convenient with the amorphous structure of nitrogen-doped activated carbon.

X-ray Photoelectron Spectroscopy (XPS). XPS was used to qualitatively analyze the functional groups on the surface of activated carbon^{59,60}. Figure 7a is the wide full XPS spectra of precursor and NDAC800. As seen from the graphs, characteristic peaks of C1s, O1s, N1s are found in NDAC800, witnessing that N have been success-

Element	NDAC600		NDAC700		NDAC800	
	Mass %	Atom %	Mass %	Atom %	Mass %	Atom %
C	74.19 ± 0.33	80.88 ± 0.36	81.38 ± 0.34	87.27 ± 0.37	76.73 ± 0.24	82.18 ± 0.26
N	8.13 ± 0.55	7.60 ± 0.52	4.21 ± 0.53	3.87 ± 0.49	9.85 ± 0.48	9.04 ± 0.44
O	11.18 ± 0.34	9.15 ± 0.28	8.41 ± 0.31	6.77 ± 0.25	8.97 ± 0.25	7.21 ± 0.20
Si	0.94 ± 0.04	0.44 ± 0.02	0.52 ± 0.04	0.24 ± 0.02	0.60 ± 0.03	0.27 ± 0.01
S	0.86 ± 0.04	0.35 ± 0.02	0.72 ± 0.04	0.29 ± 0.01	0.43 ± 0.02	0.17 ± 0.01
Cl	3.79 ± 0.08	1.40 ± 0.03	3.75 ± 0.08	1.36 ± 0.03	2.70 ± 0.05	0.98 ± 0.02
Zn	0.90 ± 0.10	0.18 ± 0.02	1.01 ± 0.11	0.20 ± 0.02	0.73 ± 0.07	0.14 ± 0.01
Total	100.00	100.00	100.00	100.00	100.00	100.00

Table 2. Element analysis of NDAC600, NDAC700, and NDAC800 using EDX analysis.

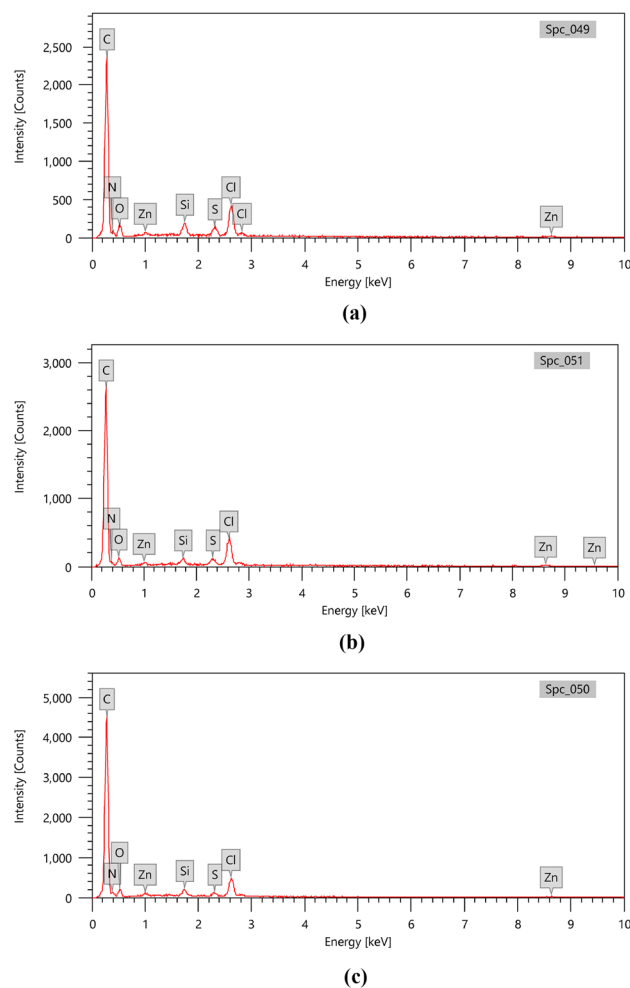


Figure 4. A EDX analysis of (a) NDAC600, (b) NDAC700, and (c) NDAC800.

fully retain on NDAC. The peaks located in 285.49, 400.33 and 533.05 eV are corresponding with C1s, N1s and O1s, respectively. Figure 7b C1s exhibits four peaks by curve fitting of the C1s spectrum. The C1s spectrum can be deconvoluted into four peaks centered at 284.51 (72.31%), 286.13 (11.15%), 287.68 eV (9.94%) and 290.18 eV (6.6%), assigned to sp^2 -C hybridized C=C bonds, C–O/C–N bonds, C=O/C=N bonds, and –O/C=O bonds respectively^{61–63}. The N1s XPS spectra of NDAC800 could be de-convoluted into two types of N-containing compounds, and results are depicted in Fig. 7c. The peaks of N1s located in 398.38 (pyridinic N) and 400.14 (pyrrolic N)^{63,64}, respectively in NDAC-600. Pyrrolic N is converted into two nitrogen-containing groups, namely 398.38 eV (pyridinic N), 400.14 eV and (pyrrolic N). The presence of pyridinic and pyrrolic N promotes the ion transport from the electrolyte to electrode material, effectively enhancing the capacitive properties. The O1s XPS spectrum of the NDAC-600 shown exhibits two peaks in Fig. 7d at 530.75 eV, and 532.54 eV, corresponding to (C=O) and (C–O).

Thermal analysis. The mixture of fish waste (60% protein content)/sawdust/zinc chloride/urea with mass ratio (5:5:5:1), subjected to a hydrothermal process at 180 °C for 5 h were analyzed for TGA and DTA. A multistage of thermochemical decomposition of sawdust was observed, as shown in Fig. 8a. The occurrence of the first weight loss of 9.63% in the temperature range of 60.39–190 °C can be attributed to the lignocellulosic material dehydration. Second mass-loss of 55.15% appears in the range between 190 and 714 °C, and the maximum mass loss occurred at 443.85 °C. The third weight mass loss of 22.83% appears in the temperature range of 714–980 °C and the maximum weight loss occurred at 790.25 °C which is may be due to the presence of unstable cellulosic fragments and the depolymerization of cellulose. The representative TGA and DTA curves of the mixture of the samples subjected to hydrothermal process at 180 °C for 5 h, is presented in the typical Fig. 8b. The TGA and DTA results indicate that, the major thermochemical decompositions take place in the temperature ranges of 25–145, 150–477, 497.86–720.77, 722.77–838.00 and 840.09–990.00 °C with weight loss 1.981, 36.35, 15.81, 5.975 and 5.313%, respectively. In the first stage, in the temperature range of 25–145 °C, it was observed that a small amount of weight loss shown in TGA curve is accompanied by a small peak in DTA curve corresponding to the release of moisture. The second stage showed a significant weight loss from 150 to 477 °C accompanied by a large peak shown in DTA curve. In the third stage, a moderate weight loss occurred within the temperature

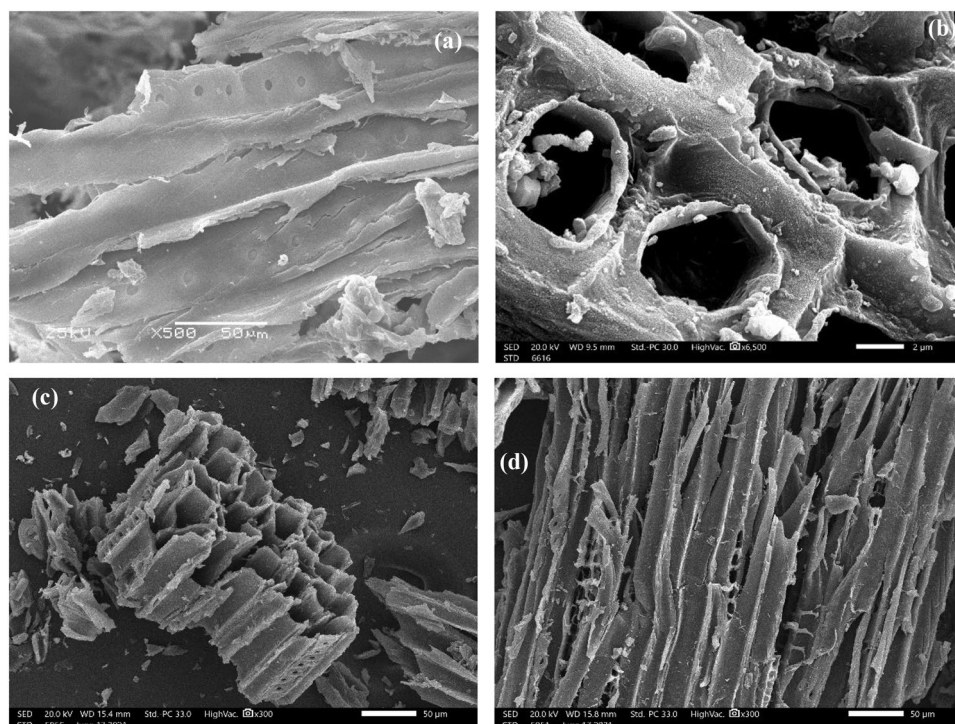


Figure 5. SEM analysis image of (a) raw sawdust, (b) NDAC800, (c) NDAC700, and (d) NDAC600.

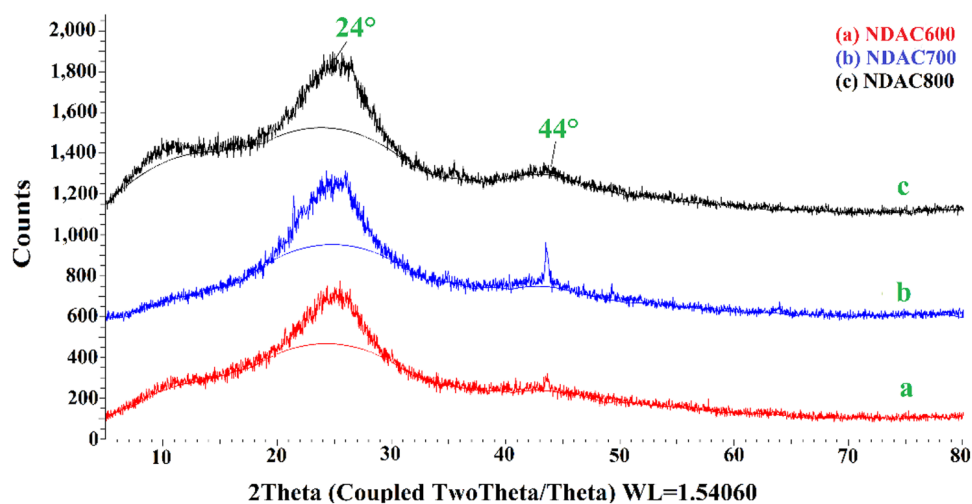


Figure 6. The XRD analyses of (a) NDAC600, (b) NDAC700 and (c) NDAC800.

changed from 497.86 to 722.77 °C. While the fourth stage showed a little weight loss of 5.975% at temperature range of 722.77–840.09 °C which may be contributed to the release of $ZnCl_2$ (melting point ~ 283 to 290 °C and boiling point of 732 °C) accompanied by a few volatiles organic compounds. The last stage showed a little weight loss of 5.313% in the temperature range between 840.09 and 990.00 °C.

Figure 9 reported the DTA and TGA analyses of the prepared NDAC600, NDAC700, and NDAC800. The first weight loss occurred for the three samples was 19.32, 22.30, and 18.27%, respectively in the temperature range of 25–150 °C which can be attributed to the water content in the samples. For the NDAC600, four more weight losses were occurred as 3.79, 4.29, 20.23, and 9.92% appears in the range between 150 and 1000 °C, and the maximum mass loss occurred at 400 to 750 °C (20.23%), which may be attributed to complete decomposition of the NDAC600. For the NDAC700 and NDAC800, almost similar two more weight losses were reported between 150 and 1000 °C, which proved that when the pyrolysis occurred at 700 and 800 °C, the produced NDACs were have almost similar thermal stability (Fig. 9). The DTA results supported the TGA analyses for the prepared

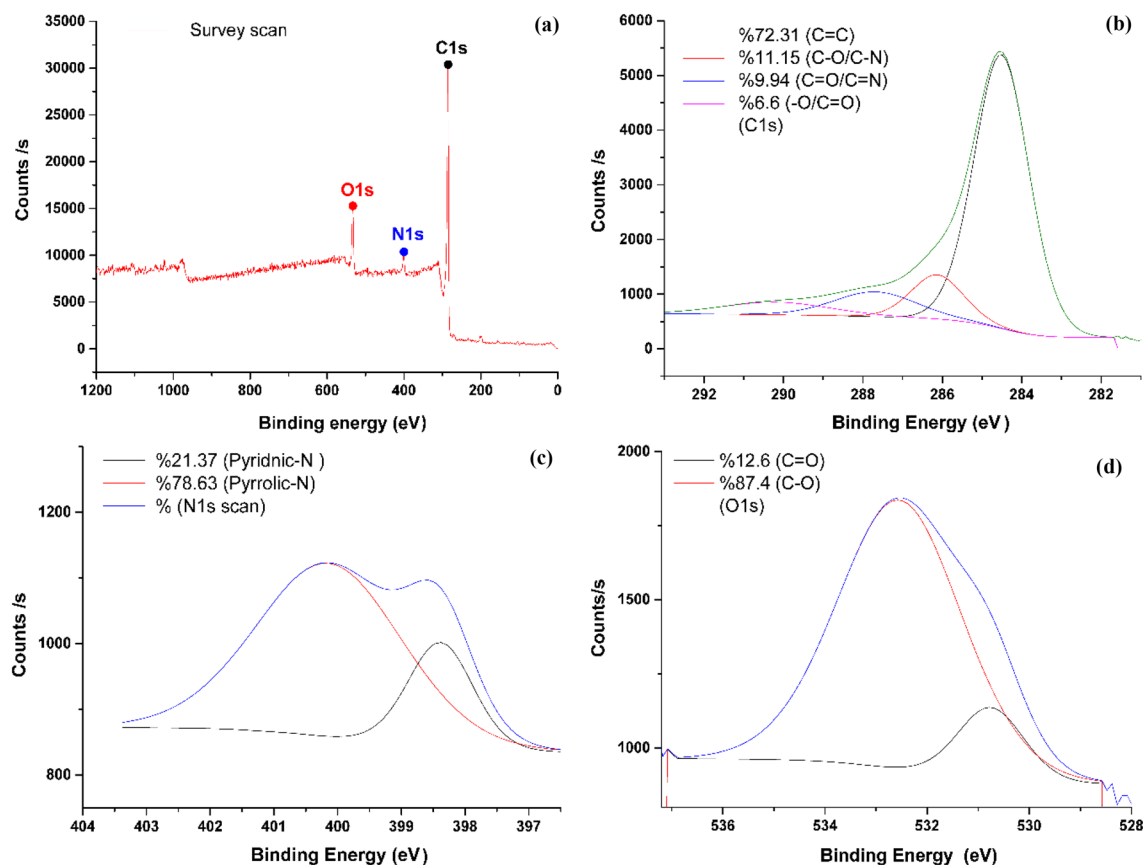


Figure 7. (a) Overview spectrum of NDAC800 with 1 eV resolution, (b) C1s, (c) N1s and (d) O1s High resolution of XPS core level spectra.

NDAC600, NDAC700, and NDAC800. In the first stage, in the temperature range of 25–150 °C, it was observed that about 20% of weight loss shown in TGA curve is accompanied by strong peaks in DTA curve corresponding to the release of moisture. The remaining stage showed a significant weight loss from 150 to 1000 °C accompanied by a multiple small peaks shown in DTA curve (Fig. 9).

Testing of prepared NDACs for the adsorption of AY36 dye. All the prepared NDACs were tested for the removal of AY36 dye from water and the more efficient was selected for further studies. The obtained results were shown in Fig. 10. The NDAC800 sample has the highest removal rate (98.37%), while NDAC600 has the lowest removal rate (88.25). Therefore, the NDAC800 was selected to investigate the AY36 dye removal through this study.

Adsorption studies of AY36 dye. *pH on AY36 dye removal.* The pH of an aqueous solution is one of the most important factors in the adsorption of cationic and anionic dyes because it influences both the surface binding sites of the adsorbent and the ionization process of the dye molecule. For this purpose, different pH values ranging from 1 to 11 were tested for the removal of the considered dye. During pH effect studies, the following parameters were kept constant (The initial AY36 dye concentrations of 100 mg/L, the NDAC800 dose of 1.0 g/L, 200 rpm agitation speed, and 25 °C temperature). During the tests, pH values were changed by adding a few drops of 0.1 M NaOH or HCl. Figure 11 shows the effect of the pH values on the removal of AY36 dye onto NDAC800. The amount of AY36 dye removal decreased with an increase in the pH value. When the pH value was changed from 1.5 to 9, the removal efficiency was decreased from 85.86 to 4.07%. While at pH = 11, the removal efficiency increased to 18.64%. The optimum pH was found to be 1.5 with the highest removal efficiency of 85.86%. The protonation state of the adsorbent may account for the higher removal efficiency of AY36 dye from NDAC800 at lower pH values^{65,66}. Electrostatic repulsion between the anionic AY36 dye molecules and the negatively charged surface of NDAC800 was produced by the increase in pH value, which decreased the positively charged sites number and raised the negatively charged sites number^{67–69}.

Contact time effect on AY36 dye removal. All transfer phenomena, including the adsorption process, unavoidably involve contact time as a fundamental characteristic. Figure 12 shows the contact time effect of the on the removal rates of AY36 dye on NDAC800 for 120 min. It is clearly shown in Fig. 12, the most of AY36 dye is removed after 10 min, and the removal percentage at 100 mg/L initial concentration of AY36 dye was 66.18% while the removal rate was 49.35% at the initial concentration 150 mg/L. After that, the removal rate tastily

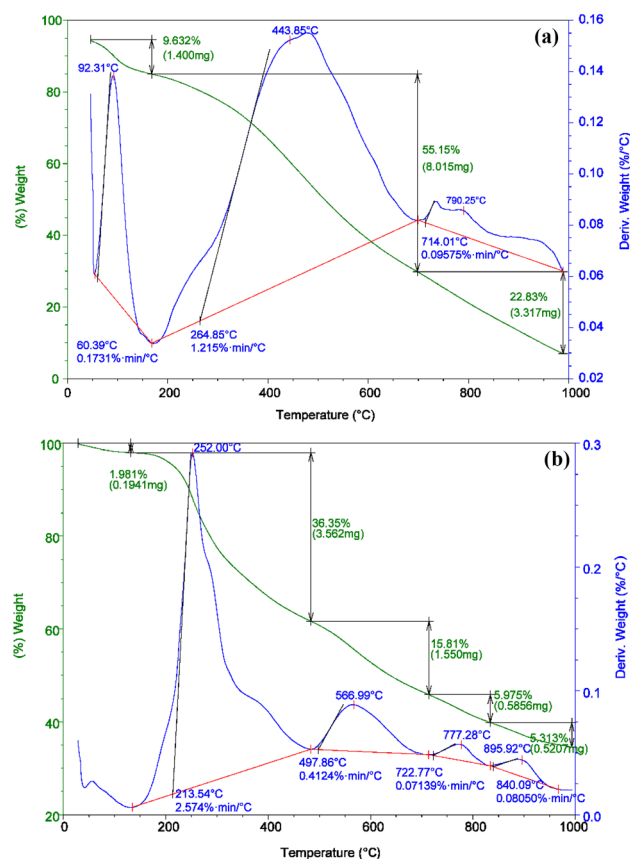


Figure 8. DTA and TGA analyses of (a) Sawdust, (b) Sawdust/fish waste/ZnCl₂/urea (5:5:5:1) mixture.

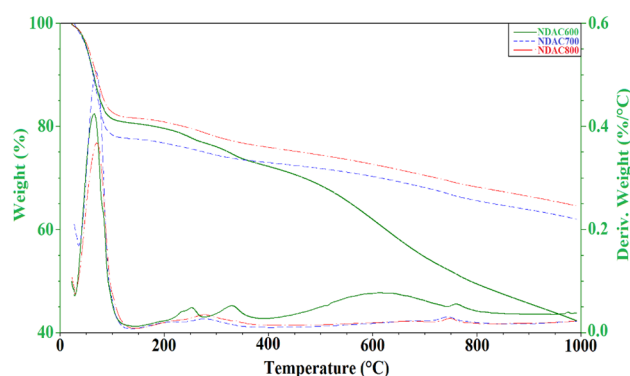


Figure 9. DTA and TGA analyses of NDAC600, NDAC700, and NDAC800.

increased until it reached the equilibrium after 120 min and became stable at 89.707 and 75.82%, respectively. At the initial concentrations of 200, 250, and 400 mg/L, the removal rate after 10 min was 36.28, 18.79, and 24.55%, respectively, and increased slowly with marginal and moderate values until it reached the equilibrium after 120 min and become 57.10, 47.96 and 41.18%, respectively. It is proved that the amount of AY36 dye that was removed by NDAC800 grew rapidly at first (helping with external surface adsorption) and then progressively over a longer period of time until equilibrium was established (contributing to internal surface adsorption). This effect was noticed due to the high concentration of the solution and all the active sites on the NDAC800 surface were initially unoccupied. After that time, there weren't many surface active sites accessible, so the amount of AY36 dye removed increased extremely slowly⁷⁰.

The AY36 dye was fast up taken onto NDAC800 to its large specific surface areas, adsorbent-adsorbate interaction, porous structures and pore volumes. This electrostatic attraction is due to the lone pair of electrons that are carried by nitrogen atoms of NDAC800 and delocalize the initial *sp*² hybrid electron cloud on the carbon skeleton, increasing both surface reactivity and electron transport.

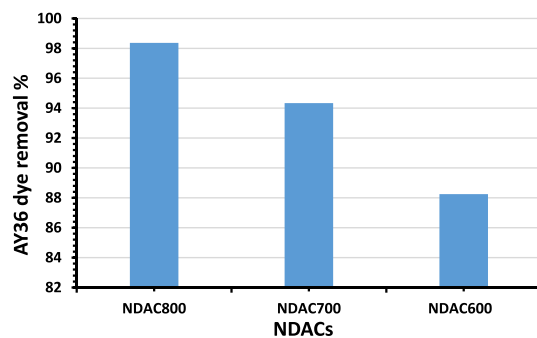


Figure 10. Removal of AY36 dye using NDACs prepared at different temperature under N_2 gas flow.

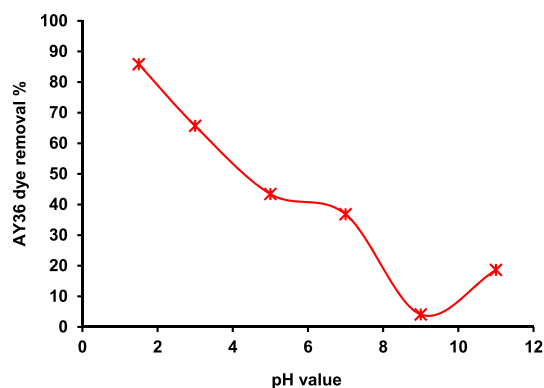


Figure 11. pH on the AY36 dye removal by NDAC800 (1.0 g/L) and 100 mg/L initial dye concentration at 25 ± 2 °C.

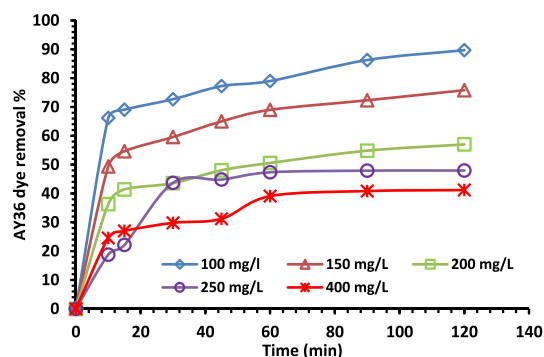


Figure 12. Effect of contact time on the removal rate of AY36 dye at different initial concentrations using 1.0 g/L of NDAC800 at 25 ± 2 °C.

Initial concentrations effect and adsorbent dosage. The initial concentrations effect of AY36 dye solutions on the removal rate was investigated. An experimental contact time of 120 min and a pH of 1.5 were chosen (determined previously) to study the effect of initial concentration (100, 150, 200, 250, and 400 mg/L) and NDAC800 dosages (0.50–2.50 g/L). Figure 13a displays the plot of Q_e (mg/g) versus initial concentration. At the adsorbent dose of 0.50 g/L and the initial dye concentration ranging from 100 to 400 mg/L, the equilibrium uptake capacity, Q_e (mg/g), increased from 137.263 to 207.639 mg/g. At the adsorbent doses of dye (1.00, 1.50, 2.00 and 2.50 g/L) and the initial dye concentration of 100–400 mg/L, the equilibrium uptake capacity, Q_e (mg/g) increased from 89.707 to 164.736, 61.625 to 156.970, 45.834 to 156.588 and 39.412 to 134.513 mg/g, respectively. It is observed that, the dye maximum adsorption capacity decreased from 207.639 to 134.513 mg/g due to increasing in NDAC800 adsorbent dosage from 0.5 to 2.5 g/L and at initial dye concentration of 400 mg/L. Figure 13b shows the plot of Q_e (mg/g) versus various NDAC800 doses (0.50–2.50 g/L) using different initial dye concentrations of (100–400 mg/L). At NDAC800 dose 0.5 g/L and the initial dye concentration of 100 mg/L, the

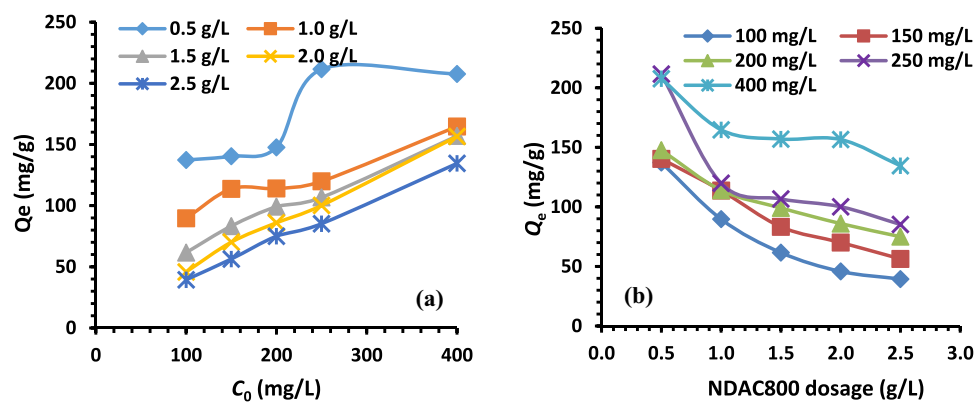


Figure 13. (a) Relation between Q_e (mg/g) and different initial concentrations of AY36 dye (100–400 mg/L) using different NDAC800 dosages (0.5–2.5 g/L); (b) plots of Q_e against different NDAC800 dosages (0.5–2.5 g/L) using different initial dye concentrations (100–400 mg/L) at 25 ± 2 °C.

Q_e decreased from 137.263 to 39.412 mg/g. At absorbent doses 1.00, 1.50, 2.00 and 2.50 g/L of NDAC800 and the initial concentration of AY36 dye 150, 200, 250, and 400 mg/L, the Q_e decreased from 140.357 to 56.359, 147.652 to 74.987, 211.522 to 85.240 and 207.639 to 134.513 mg/g, respectively. From the results, it can be deduced that the equilibrium uptake capacity (Q_e) at initial concentration ranging from 100 to 250 mg/L increases from 137.263 to 211.522 mg/g, while at initial dye concentration 400 mg/L decreased to 207.639 mg/g for an increase in the AY36 dye concentration from 100 to 400 mg/L using NDAC800 dose 0.5 g/L. Q_e at 250 mg/L as dye initial concentration and NDAC800 dosage 0.5 g/L possessed the highest value, 211.522 mg/g. Because more vacant adsorption sites are available due to rising the amount of NDAC, more dye may be absorbed, resulting in a rise in dye removal percentage.

The increase in NDAC800 dose causes a decrease in the amount of AY36 dye adsorbed onto the unit weight of NDAC800, which results in a lower solute concentration, and this decrease in AY36 dye adsorbed onto NDAC800 dose weight may be the cause of the decrease in Q_e value (concentration gradient or splitting effect) between sorbets and sorbent. The initial concentration gradient between the solid adsorbent and the bulk liquid can be used to explain this. The driving force, or initial AY36 dye concentration incline, is likely to cause a rise in the amount of dye absorbed per unit weight of adsorbent. However, in this instance, the initial concentration incline between the adsorption vacant sites of NDAC800 and the concentration of AY36 dye solutions gets smaller with increasing adsorbent mass, directing to a decrease in q_e value for a fixed volume of dye solution and initial dye concentration. It can be seen from Fig. 13a and b that for all of the adsorbent masses examined, the concentration in AY36 dye solution was greater than the maximum number of unoccupied sites that could be found at the surface of the adsorbent. But it was nevertheless discovered that the Q_e value fell as NDAC800 mass rose. This impact may be ascribed to a decrease in the adsorbent's overall surface area, which is likely the result of aggregation during the adsorption process^{71,72}.

AY36 dye adsorption isotherms models. Isotherm of adsorption, a useful tool, often describes the mechanisms controlling the retention or mobility of material from aqueous porous media or aquatic habitats to a solid phase at a constant conditions^{73,74}. Once an adsorbate-containing phase has been in contact with the adsorbent for enough time, its adsorbate concentration in the bulk solution becomes in a dynamic balance with the interface concentration; equilibrium of the adsorption (the ratio between the amount of pollutant adsorbed and the amount remaining in the solution) is established^{75,76}. The mathematical relationship, which is frequently used and shown by expressing the solid phase versus its remaining liquid concentration⁷⁷, typically plays an important role in the modelling analysis, working design, and practical application of adsorption methods. Understanding the adsorption mechanism, surface properties, and degree of adsorbent affinities is possible due to the parameters of this substance's physicochemistry and the underlying thermodynamic theories⁷⁸.

Numerous adsorption isotherm models, namely Langmuir (LIM), Freundlich (FIM), Dubinin-Radushkevich (DRIM), Temkin (TIM), and Halsey isotherm (HIM), have been developed over time to analyse experimental data^{78–80}. The first method mentioned is kinetic consideration.

While thermodynamics, the base of the second approach, can give an outline for generating several types of adsorption isotherm models^{81,82} and potential theory. The third approach, often transmits the primary notion in the production of the distinguishing curve⁸³. However, the derivation in more than one way, which points to the discrepancy in the physical interpretation of the model parameters, is an intriguing development in isotherm modeling. The experimental results in this study were investigated using the above mentioned equilibrium isotherm models⁷⁸.

Langmuir isotherm model (LIM). The LIM⁸⁰ undertakes uniform energies of removal of a solute from a fluid solution onto a surface comprising a definite number of identical sites as a monolayer adsorption with no adsorbate transmigration into the surface plane⁸⁴. Therefore, LIM was selected to estimate the maximum adsorption capacity (Q_m , mg/g) of complete monolayer coverage on the surface of sorbent. LIM is expressed by Eq. (4)

(Table 3), where q_e (mg/g) is the mono-layer adsorption capacity of adsorbent at equilibrium and K_L (L/mg) is the LIM adsorption constant. Therefore, a plot of C_e/q_e versus C_e gives a straight line of slope $1/Q_m$ and intercepts $1/(Q_m K_L)$. The LIM plot is shown Fig. 2Sa in supplementary material, and the LIM data are given in Table 4.

Freundlich isotherm model (FIM). The FIM is the initially reported equation investigating the adsorption process⁸⁵. The FIM expression assumes that because it is an exponential equation, the concentration of adsorbate on the adsorbent surface increases as well as the adsorbate concentration does. The FIM can be expressed as Eq. (5) (Table 3), where K_F and n are the FIM adsorption constants, which can be measured by the linear plot of $\log q_e$ versus $\log C_e$. $1/n$ is a constant revealing of the intensity of the adsorption of dye onto the surface heterogeneity sorbent, becoming more heterogeneous as its value gets closer to zero. A value of $1/n$ below one indicates a normal LIM, while $1/n$ above one is revealing cooperative adsorption. The FIM plot is presented in Fig. 2Sb in supplementary material, and the FIM parameters are given in Table 4.

Temkin isotherm model (TIM). The TIM made the assumption that all of the molecules in the layer's heat of adsorption decreased linearly with coverage as a result of interactions between adsorbents and adsorbates and that the adsorption was characterized by a uniform distribution of binding energies up to a maximum binding energy^{86,87}. TIM is expressed as Eq. (6), where A and B are TIM constants, R is the gas constant, and T is the absolute temperature. The applicability of the isotherm was confirmed by a linear plot of q_e versus $\ln C_e$, which can be used to determine the constants A and B as shown in Fig. 2Sc in supplementary material and reported in Table 4.

Dubinin-Radushkevich model (DRIM). The DRIM^{88,89} assesses the apparent porosity free energy and adsorption characteristics. The dose of DRIM not undertakes a constant sorption potential or homogeneous surface. The DRIM can be written as Eq. (7) (Table 3)⁹⁰, where β (mmol²/J²) is a coefficient corresponding to the adsorption mean free energy of, q_m (mmol/g) is the maximum adsorption capacity and ϵ (J/mmol) is the polanyi potential which is written as: $\epsilon = RT(1 + 1/C_e)$. The DRIM plot is shown in Fig. 2Sd in supplementary material, and the DRIM parameters are given in Table 4.

Isotherm models	Linear equation	Equation no.
Langmuir	$\frac{C_e}{q_e} = \frac{1}{K_L Q_m} + \frac{1}{Q_m} C_e$	(4)
Freundlich	$\log q_e = \log K_F + \frac{1}{n} \log C_e$	(5)
Temkin	$q_e = \frac{RT}{B} \ln A + \frac{RT}{B} \ln C_e$	(6)
Dubinin-Radushkevich	$\ln q_e = \ln q_m - \beta \epsilon^2$	(7)
Halsey	$\ln q_e = \frac{1}{n} \ln k + \frac{1}{n} \ln C_e$	(8)

Table 3. The equations of isotherm models (IM).

Isotherm models	IM parameters	NDAC800 (g/L)				
		0.5	1.0	1.5	2.0	2.5
Langmuir	Q_m (mg/g)	232.56	169.49	169.49	188.68	142.86
	$K_a \times 10^3$	25.34	38.89	35.04	36.53	86.85
	R^2	0.947	0.948	0.932	0.892	0.897
Freundlich	$1/n$	0.21	0.16	0.28	0.42	0.30
	K_F (mg ^{1-1/n} L ^{1/n} /g)	63.61	60.62	33.88	21.90	32.94
	R^2	0.619	0.815	0.946	0.895	0.921
Temkin	A_T	1.19	7.89	0.93	0.45	2.53
	B_T	34.93	19.40	27.59	37.91	22.29
	R^2	0.600	0.748	0.861	0.863	0.810
Dubinin-Radushkevich	Q_m (mol/kg)	178.70	128.09	111.37	117.08	84.88
	$K \times 10^6$ (mol/kJ) ²	48,800	6900	6500	10,900	500
	E (kJ/mol)	3.20	8.51	8.77	6.77	31.62
	R^2	0.327	0.537	0.609	0.780	0.565
Halsey isotherm	$1/n_H$	0.2053	0.1611	0.2796	0.4197	0.3025
	K_H	6.09E+08	1.16E+11	2.96E+05	1.56E+03	1.04E+05
	R^2	0.6189	0.8148	0.9458	0.8895	0.9208

Table 4. Isotherm models investigation data of AY36 dye adsorption of 100–400 mg/L as initial dye concentration onto 0.5–2.5 g/L NDAC800 doses at 25 ± 2 °C.

Halsey model (HIM). Multilayer adsorption, and heteroporous substances may fit the HIM^{91,92}. HIM is expressed as Eq. (8) (Table 3), where K and n are the HIM adsorption constants that can be obtained from the linear plot of $\ln q_e$ versus $\ln C_e$ as shown in Fig. 2Se in supplementary material and the obtained data were included in Table 4.

Error functions investigation (EFI). In recent years, there have seen a rise in the use of linear regression, which is the most effective method for determining the best fitting^{78,93}, mathematically analyzing adsorption systems, measuring the distribution of adsorbates⁹⁴, and confirming the reliability and theoretical premises of an isotherm model⁹⁵.

Because of the characteristic bias caused by the transformation in this study, which rides towards a variety of parameter approximation errors and fits distortion, a number of mathematically rigorous error functions (including the hybrid function fractional error (HYBRID), ARE (average relative error), X^2 (nonlinear chi-square test), MPSD (Marquardt's percent standard deviation), ERRSQ (sum square error), EABS (sum of absolute errors), APE (average percentage errors), and root mean square error) have done. Based on its convergence criteria, nonlinear regression often includes either minimization or maximization of the error distribution (between the experimental data and the predicted isotherm)⁹⁶. This is in contrast to linearization models. Despite the fact that the Sum Square Error (ERRSQ) is the most frequently employed error function^{78,97}, the magnitude and squares of the errors tend to grow at the liquid-phase higher-end concentration ranges, demonstrating a better fit for parameters derivation of the isotherm⁹⁸. Equation (9) represents ERRSQ (Table 5).

The development of the error function improved the HYBRID fit at low concentrations. Here, each value of ERRSQ is divided by the solid-phase concentration of the experimental with a term for the degrees number of freedom (the data point number minus the parameters number in the isotherm equation) built into the system⁹⁹. ARE model¹⁰⁰ shows a propensity to underestimate or overestimate the experimental data, and aims to reduce the fractional error distribution over the whole concentration range under study. The ERRSQ function and the sum of absolute errors (EABS) both use an approach where an increase in errors will result in a better fit and a bias toward data with high concentrations¹⁰¹. A number of scholars have previously used MPSD (Eq. 13) error function¹⁰² in the isotherm investigations^{103–106}. It resembles a modified geometric mean error distribution in some ways, depending on the system's degree of freedom¹⁰⁰. The nonlinear chi-square test, which can be calculated by comparing the sum squared differences between calculated and experimental data and dividing each squared difference by its corresponding value, is a statistical tool required for the best-fit of an adsorption system (X^2 is expressed as Eq. (14)). While a higher number reflects the variance of the experimental data, a smaller X^2 value indicates its similarities⁹⁵. According to Eq. (15), the average percentage errors (APE) show how well the observed and anticipated values of adsorption capacity used to create isotherm curves match together⁹⁹. Equation (16) gives the root mean square errors (RMS)⁹⁹ (Table 5).

The q_e (211.552 mg/g) and the Q_m (232.56 mg/g) are in excellent agreement, and an evaluation of the isotherms based on their coefficient of determination (R^2) (0.948) revealed that the LIM is the best model fits the data (Table 6). However, when comparing the isotherms based on error functions, Temkin has the least error functions, roughly equal. However, the adsorption of the AY36 dye onto NDAC800 could be adequately predicted by the two isotherm models, according to the data reported above.

AY36 dye adsorption kinetic models. The rate controlling the process of adsorption was studied using a number of kinetic models, including mass transfer, diffusion control, and chemical reaction. The kinetics of AY36 dye adsorption onto NDAC800 was investigated in order to choose the best working conditions for

EM name	Error equation	Equation no.
ERRSQ	$ERRSQ = \sum_{i=1}^n (q_{e, isotherm} - q_{e, cal})^2$	(9)
HYBRID	$Hybrid = \frac{100}{p-n} \sum_{i=1}^p \left(\frac{(q_{e, isotherm} - q_{e, cal})^2}{q_{e, isotherm}} \right) i$	(10)
ARE	$ARE = \frac{100}{n} + \sum_{i=1}^n \left \frac{q_{e, isotherm} - q_{e, cal}}{q_{e, isotherm}} \right i$	(11)
EABS	$EABS = \sum_{i=1}^n q_{e, isotherm} - q_{e, cal} i$	(12)
MPSD	$MPSD = 100 \times \sqrt{\frac{\sum_{i=1}^n \left(\frac{q_{e, isotherm} - q_{e, cal}}{q_{e, isotherm}} \right)^2}{n-p}}$	(13)
X^2	$X^2 = \sum_{i=1}^n \left(\frac{(q_{e, meas} - q_{e, cal})^2}{q_{e, exp}} \right)$	(14)
APE	$APE\% = \frac{100}{n} \times \sum_{i=1}^n \left \frac{q_{e, isotherm} - q_{e, cal}}{q_{e, isotherm}} \right i$	(15)
RMS	$RMS = 100 \times \sqrt{\frac{\sum_{i=1}^n \left(1 - \frac{q_{e, cal}}{q_{e, isotherm}} \right)^2}{n}}$	(16)

Table 5. Error functions models applied to investigate of the various isotherm models applicability.

IM name	APE%	X ²	ERRSQ	Hybrid	MPSD	ARE	EABS	RMS
Langmuir	0.10	1.90	213.30	8.27	0.54	0.10	73.02	0.52
Freundlich	0.03	0.15	16.35	0.63	0.15	0.03	20.22	0.14
Halsey	10.45	5257.84	162,027.72	22,860.18	54.47	10.45	2012.63	52.25
Temkin	0.00	0.00	0.00	0.00	0.00	0.00	0.02	0.00
D-R	0.08	1.11	124.66	4.83	0.42	0.08	55.83	0.40

Table 6. The isotherm models Error function analysis of the AY36 dye adsorption of different C₀ (100–400 mg/L) onto NDAC800 different doses (0.5–2.5 g/L) at 25 ± 2 °C.

a full-scale batch process because the parameters of kinetic are important for the adsorption rate prediction and provide crucial evidence for scheming and modeling the adsorption processes. Consequently, pseudo-first order (PFOM)^{107,108}, pseudo-second-order (PSOM)¹⁰⁹, Elovich (EM)^{110–112}, intraparticle diffusion (IDM) and

Model name	Model Equation	Equation no.
PFO	$\log(q_e - q_t) = \log q_e - \frac{K_1}{2.303} t$	(17)
PSO	$\frac{t}{q_t} = \frac{1}{K_2 q_e^2} + \frac{t}{q_e}$	(18)
Elovich kinetic	$q_t = \frac{1}{\beta} \ln(\alpha \beta) + \frac{1}{\beta} \ln(t)$	(19)
Intraparticle diffusion	$q_t = K_{df} t^{0.5} + C$	(20)
Film diffusion	$\ln(1 - F) = K_{FD}(t)$	(21)

Table 7. The used adsorption kinetic models equations.

Parameter			PFOM			PSOM		
NDAC800 (g/L)	AY36 (mg/L)	q _e (exp.)	q _e (calc.)	k ₁ × 10 ³	R ²	q _e (calc.)	k ₂ × 10 ³	R ²
0.5	100	137.26	81.55	30.86	0.977	149.25	0.601	0.998
	150	140.36	64.48	33.85	0.904	147.06	0.978	0.996
	200	147.65	125.46	38.46	0.961	166.67	0.388	0.994
	250	211.52	372.48	57.34	0.874	294.12	0.087	0.949
	400	207.64	252.70	27.64	0.798	303.03	0.052	0.796
1.0	100	89.71	31.98	22.57	0.946	92.59	1.551	0.996
	150	113.73	49.33	25.10	0.996	119.05	1.008	0.998
	200	114.02	54.80	26.71	0.976	120.48	0.902	0.997
	250	119.90	172.86	78.30	0.985	140.85	0.454	0.982
	400	164.74	153.53	47.90	0.908	181.82	0.442	0.989
1.5	100	61.63	20.34	39.38	0.861	63.69	3.567	0.998
	150	83.29	26.01	17.96	0.765	85.47	1.667	0.994
	200	99.12	42.70	22.11	0.983	104.17	1.054	0.998
	250	106.68	71.61	24.41	0.829	119.05	0.456	0.974
	400	156.97	117.14	31.78	0.914	175.44	0.371	0.988
2.0	100	45.83	0.54	17.04	0.277	44.64	94.672	0.999
	150	70.13	20.94	39.84	0.860	70.92	4.873	0.999
	200	86.00	32.67	22.11	0.902	90.09	1.341	0.994
	250	100.14	53.27	31.32	0.978	107.53	0.990	0.999
	400	156.59	65.45	32.24	0.891	163.93	0.926	0.996
2.5	100	39.41	2.99	22.11	0.894	39.68	20.033	1.000
	150	56.36	5.79	35.24	0.257	55.87	16.101	0.999
	200	74.99	30.01	24.87	0.962	78.13	1.682	0.997
	250	85.24	30.08	21.42	0.877	88.50	1.590	0.999
	400	134.51	67.20	34.31	0.819	140.85	0.923	0.994

Table 8. PFOM and PSOM rate constants as well as the experimental and calculated q_e values of AY36 dye adsorption of 100–400 mg/L as C₀ and 0.5–2.5 g/L NDAC800 doses at 25 ± 2 °C.

NDAC800 (g/L)	AY36 (mg/L)	EM			IPDM			FDM		
		β	α	R^2	K_{diff}	C	R^2	K_{FD}	C	R^2
0.5	100	0.04	6.67E+01	0.987	7.49	60.82	0.956	0.03	0.52	0.977
	150	0.07	1.15E+03	0.938	4.95	88.38	0.962	0.03	0.78	0.904
	200	0.03	3.24E+01	0.963	9.81	48.78	0.933	0.04	0.16	0.961
	250	0.015	1.59E+01	0.969	20.88	9.12	0.847	0.00	0.92	0.000
	400	0.02	1.17E+01	0.848	19.90	13.55	0.921	0.03	0.20	0.798
1.0	100	0.11	9.83E+02	0.956	3.02	56.69	0.994	0.02	1.03	0.946
	150	0.06	1.74E+02	0.994	4.99	61.74	0.972	0.03	0.84	0.996
	200	0.06	1.48E+02	0.979	5.15	59.91	0.975	0.03	0.73	0.975
	250	0.03	1.71E+01	0.846	9.46	33.29	0.716	0.08	0.37	0.985
	400	0.03	7.54E+01	0.919	9.28	70.66	0.924	0.05	0.07	0.908
1.5	100	0.13	3.18E+02	0.772	2.26	40.25	0.685	0.02	2.26	0.254
	150	0.11	4.82E+02	0.843	2.99	50.76	0.844	0.02	1.16	0.765
	200	0.07	9.86E+01	0.995	4.63	50.45	0.963	0.02	0.84	0.983
	250	0.05	2.15E+01	0.860	6.88	32.66	0.844	0.02	0.40	0.829
	400	0.03	5.20E+01	0.941	9.31	58.67	0.974	0.03	0.29	0.914
2.0	100	-1.81	1.29E-37	0.249	-0.15	45.68	0.180	0.01	2.69	0.026
	150	0.15	2.77E+03	0.884	1.97	50.65	0.767	0.01	2.39	0.012
	200	0.10	2.69E+02	0.846	3.40	49.54	0.865	0.02	0.97	0.902
	250	0.06	6.71E+01	0.961	5.09	48.85	0.898	0.03	0.63	0.978
	400	0.07	3.00E+03	0.904	5.04	102.92	0.953	0.03	0.87	0.891
2.5	100	1.24	9.00E+18	0.885	0.27	36.40	0.966	0.02	2.58	0.894
	150	0.26	1.20E+05	0.625	1.05	46.11	0.467	0.03	1.73	0.142
	200	0.11	2.83E+02	0.959	2.88	44.38	0.962	0.02	0.92	0.962
	250	0.09	1.63E+02	0.973	3.55	48.36	0.911	0.02	1.04	0.873
	400	0.07	1.33E+03	0.883	4.68	83.84	0.954	0.03	0.69	0.819

Table 9. EM, IPDM, and FDM results of AY36 dye adsorption of 100–400 mg/L beginning concentrations onto 0.5–2.5 g/L NDAC800 doses at 25 ± 2 °C.

film diffusion (FDM) kinetic models^{113,114} were used for AY36 dye adsorption onto NDAC800 (Table 7). The conventionality between the model-predicted values and experimental data was expressed by the R^2 (correlation coefficients), as shown in Fig. 3Sa–e in supplementary material and Tables 8, 9.

Pseudo-first-order model (PFOM). The adsorption rate constant was measured by the Lagergren PFOM¹⁰⁸, which is the initial known model describing the adsorption rate based on the adsorption capacity. The pseudo-first-order (PFO) kinetic model is shown by Eq. (17) as q_t and q_e (mg/g) are the quantities of ion adsorbed at time t and equilibrium, respectively, and k_1 (min^{-1}) is the PFO rate constant of adsorption process. The slope and intercept of the plots of $\log(q_e - q_t)$ versus t were used to calculate the k_1 and q_e (Fig. 3Sa in supplementary material).

Pseudo-second-order model (PSOM). According to PSOM, the number of accessible sites on the adsorbent directly relates to the rate of solute adsorption. Additionally, the amount of solute on the adsorbent's surface affects the reaction rate. The $q_e - q_t$ (driving force) is relational to the active sites number available on the adsorbent^{115,116}. The PSOM is shown by Eq. (18), where k_2 (g/mg min) is the equilibrium rate constant of PSOM adsorption¹¹⁷. If the PSOM is appropriate, the plot of t/q_t versus t shows a linear relationship, and the k_2 and q_e can be obtained from the slope and intercept of the line, respectively (Fig. 3Sb in supplementary material).

Elovich model (EM). The EM aids in predicting a system's activation and deactivation energy as well as mass and surface diffusion. The model has been meaningfully applied to wastewater processing despite its initial application in gaseous systems. The model posits that as the amount of deposited solute increases, the rate of solute adsorption reduces exponentially^{118,119}. EM undertakes the presence of heterogeneous active sites on adsorbent material¹²⁰. EM is presented by Eq. (19), where α (mg/g min) and β (g/mg) are the beginning sorption rate constant and the surface coverage and activation energy for chemisorption, respectively. These constants can be calculated from the slope and intercept of q_t versus $\ln t$ plot following the model equation (Fig. 3Sc in supplementary material).

Intra-particle diffusion model (IPDM). It is reasonable to suppose that the mechanism of adsorption for any dye removal using a solid phase material involves the subsequent four steps: (1) the transfer of color from a solution to the top of a solid phase (bulk diffusion); (2) the passage of dye through the boundary layer from the surface

of the solid phase (FD); (3) the transfer of dye between the solid phase's surface and its particles' inner pores (intraparticle (IPD) or pore diffusion (PD)); and (4) the dye's adsorption at an active site on the surface of the solid phase (Chemical reaction such as ion-exchange, complexation and chelation). Usually, the mass transfer rates between the liquid phase and the IPD control dye adsorption¹²¹.

IPD may be the rate-regulating step in an experiment that uses a batch method and rapid stirring¹²². The IPDM was also investigated using Eq. (20)¹²³, where k_{dif} is the IPD rate constant (mg/g min^{1/2}) (Fig. 3Sd in supplementary material).

Film diffusion model (FDM). Film diffusion (FD) is the adsorbate diffusion across the liquid film surrounding the particle of the adsorbent. FDM is expressed by Eq. (21), where K_{FD} is the external film mass transfer coefficient and $F = q_t/q_e$. The constant K_{FD} can be calculated from the slope and intercept of the $\ln(1-F)$ versus plot (Fig. 3Se in supplementary material)¹²⁴.

The best fit kinetic model for the AY36 dye adsorption onto NDAC800 was the pseudo-second-order rate because PSOM rate results gave the highest determination coefficient ($R^2 = 1$). According to the LIM and TIM adsorption isotherm models and the PSOM, it can be suggested that the first step involved the electrostatic attraction between the ions of hydrogen in the bulk solution and the equivalent negatively active sites on the self-doping activated carbon. This possessed numerous numbers of lone pairs of electrons of nitrogen atoms, then the AY36 dye adsorbed onto the surface of the positively self-doping activated carbon, and it formed a detectable adsorption monolayer. This first monolayer is most often formed for large species like dye molecules (AY36 dye), which cannot be penetrated through the micropores (mean pore diameter 1.9668 nm) according to specific surface area study and strong chemisorption onto a surface of the NDAC800 may be occurred. During the adsorption process, the adsorption heat varies with coverage of the amount of AY36 dye due adsorbate interactions, and then, the rate limiting step may be chemisorption involved through electrons involvement or exchange between the Acid Yellow 36 dye and the positively self-doping activated carbon.

Comparison results of Q_m of AY36 dye compared to those found in literature. The Q_m of AY36 dye removal using various adsorbents summarised in the literature were compared to the NDAC600 adsorbent (Table 10). This demonstrated that NDAC800 was effective for the adsorption of AY36 dye. The NDAC800 shows Q_m (232.56 mg/g), which is comparable to those reported in Table 10 for various adsorbent for the AY36 dye removal from water. It was noticed that the NDAC800 was much more effective in relation to other adsorbents used for the AY36 dye removal.

Two commercial activated carbons (Fisher Scientific UK Charcoal activated code: C/4040/60 and ADWIC Egypt Charcoal activated powder) were tested in removing of AY36 dye ion from water compared with prepared

Precursor	Q_m (mg/g)	References
NDAC800	232.56	This study
Green nanoceria (GN) and GN-NH ₂ (AGN) from <i>Prosopis juliflora</i> leaves extract	GN (16.39) AGN (26.95)	31
Superabsorbent hydrogel of Poly(3-acrylamidopropyl)-trimethylammonium chloride-co-N,N-DMA	199.96	125
AC from peanut shells	66.70	126
Refused tea waste activated carbon	71.97	127
Date Seed as a biosorbent	22.07	128

Table 10. Comparison of the AY36 dye removal by NDAC800 with various adsorbents.

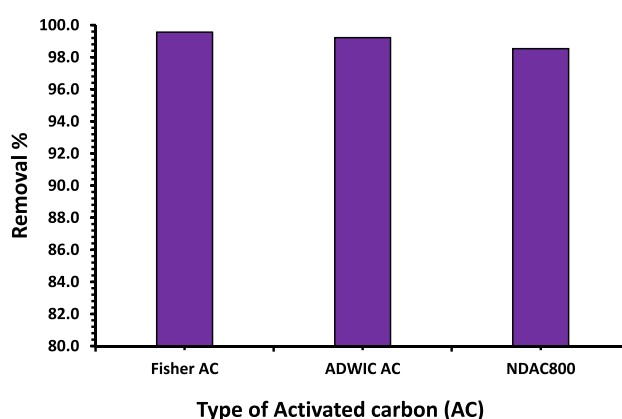


Figure 14. Removal % of AY36 dye using Fisher AC, ADWIC AC and NDAC800 using 2.5 g/L as adsorbent dose and 100 mg/L as initial dye concentration at 25 °C for 120 min.

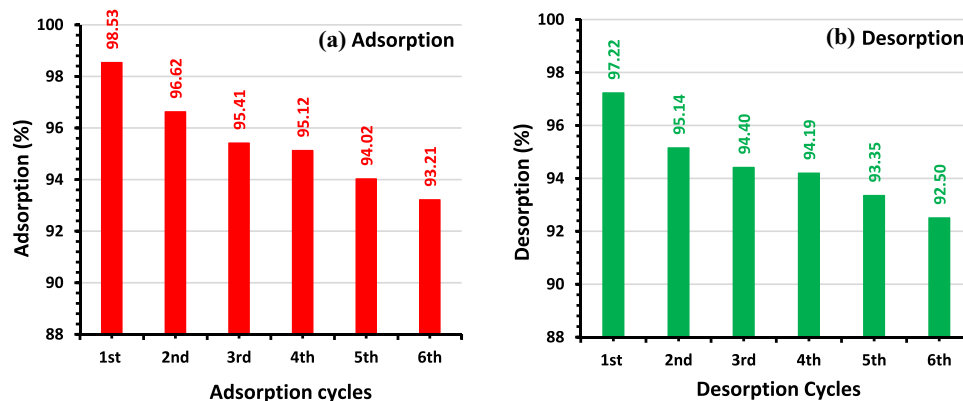


Figure 15. The effect of the regeneration rounds (cycles) (a) adsorption percentage of AY36 dye ion by NDAC800 and (b) desorption % of AY36 dye ion from NDAC800 using 2.5 g/L of NDAC800 dose and 100 mg/L, C_0 of AY36 dye ion at 25 ± 2 °C.

NDAC800 (Fig. 14). The maximum removal % of AY36 dye obtained by the commercial activated carbons was ~99.56 and 99.22%, which are very closed to that obtained by NDAC800 (98.53).

Regeneration of NDAC800. Regeneration is a commonly utilized method for the adsorption of effluents from water that is critically dependent on the reuse or recycling of adsorbent components, and the economics of this technology are also heavily dependent on this reuse or recycling. The chemical regeneration process was utilized in regenerating the depleted NDAC800. The NDAC800 was regenerated (recycled) by washing it in 0.1 M NaOH solution, 0.1 M HCl solution, clean water at high temperature, and drying it. It was noticed that the maximum adsorption % of AY36 dye ion by NDAC800 was 93.21% after six regeneration rounds (cycles) (Fig. 15a), indicating that activated NDAC800 can regenerate. The maximum desorption % of AY36 dye ion from NDAC800 after six desorption cycles was 92.50% (Fig. 15b).

Conclusion

We have successfully described an efficient, eco-friendly, cheap and simple method for preparing self-doping activated carbons via hydrothermal and pyrolysis processes at 600, 700 and 800 °C. The NDAC prepared at 800 °C (NDAC800) exhibited a high adsorption capacity of AY36 dye at equilibrium ($Q_e = 211.522$ mg/g), and 1.0 g/L of NDAC800 could easily absorb 66.18% of 100 mg/L of anionic dye AY36 within 10 min. In addition, nitrogen atoms were successfully doped into the activated carbon skeleton with nitrogen content 9.85% after carbonization. The specific surface area of NDAC800 reached 727.34 m²/g with micropores (mean pore diameter = 1.966 nm). Studies on the NDAC800's surface chemistry showed that the acidic functionality predominated over the basic functionality. NDAC800 possesses a high specific surface area, high nitrogen content and micro-porous materials. The optimum pH value of AY36 dye removal was 1.5, with a removal efficiency of 85.86%. The obtained Q_m from LIM was 232.522 mg/g. The adsorption kinetics of AY36 dye onto NDAC800 was best described using a PSOM, indicating that the AY36 dye adsorption mechanism onto NDAC800 is governed by chemisorption. The adsorption data were defined well by LIM and TIM. This method can handle the issues from the disposal of dye wastewater and turn the waste, like a fish waste (60% protein) and sawdust, into valuable materials.

Data availability

The datasets used in this investigation are accessible for review upon request from the corresponding author of the paper.

Received: 5 November 2022; Accepted: 6 April 2023

Published online: 11 April 2023

References

- Sleiman, M., Vildoza, D., Ferronato, C. & Chovelon, J. M. Photocatalytic degradation of azo dye Metanil Yellow: Optimization and kinetic modeling using a chemometric approach. *Appl. Catal. B: Environ.* **77**(1–2), 1–11 (2007).
- Sharma, U. K. *et al.* Ameliorating efficacy of eugenol against metanil yellow induced toxicity in albino Wistar rats. *Food Chem. Toxicol.* **126**, 34–40 (2019).
- Nakano, N., Yamamoto, A. & Nagashima, K. Development of a monitoring system for vinyl chloride gas in air by using an HCl monitoring tape and pyrolyzer. *Talanta* **43**(3), 459–463 (1996).
- Ramchandani, S., Das, M., Joshi, A. & Khanna, S. K. Effect of oral and parenteral administration of metanil yellow on some hepatic and intestinal biochemical parameters. *J. Appl. Toxicol.* **17**(1), 85–91 (1997).
- El Nemr, A. Impact, monitoring and management of environmental pollution. In *Pollution Science, Technology and Abatement Series* 683 (Nova Science Publishers, 2010).
- Sudarni, D. H. A. *et al.* Malachite green removal by activated potassium hydroxide clove leaves agro-waste biosorbent: Characterization, kinetics, isotherms and thermodynamics studies. *Adsorpt. Sci. Technol.* **1145312**, 1–15. <https://doi.org/10.1155/2021/1145312> (2021).

7. Hassaan, M., El Katory, M., Ali, R. M. & El Nemr, A. Photocatalytic degradation of reactive black 5 using Photo-Fenton and ZnO nanoparticles under UV irradiation. *Egypt. J. Chem.* **63**(4), 17–18 (2020).
8. Ama, O., Wilson, A. & Ray, S. Photoelectrochemical degradation of methylene blue dye under visible light irradiation using EG/Ag-ZrO₂ nanocomposite electrodes. *Int. J. Electrochem. Sci.* **14**, 9982–10001. [https://doi.org/10.1016/s1001-0742\(10\)60489-5](https://doi.org/10.1016/s1001-0742(10)60489-5) (2018).
9. El Nemr, A., Helmy, E. T., Gomaa, E. A., Eldafrawy, S. & Mousa, M. Photocatalytic and biological activities of undoped and doped TiO₂ prepared by Green method for water treatment. *J. Environ. Chem. Eng.* **7**, 103385. <https://doi.org/10.1016/j.jece.2019.103385> (2019).
10. Aigbe, U. O., Das, R., Ho, W. H., Srinivasu, V. & Maity, A. A novel method for removal of Cr (VI) using polypyrrole magnetic nanocomposite in the presence of unsteady magnetic fields. *Sep. Purif. Technol.* **194**, 377–387. <https://doi.org/10.1016/j.seppur.2017.11.057> (2018).
11. El Nemr, A. *Non-conventional Textile Waste Water Treatment 267* (Nova Science Publishers Inc, 2012).
12. Onyancha, R. B., Aigbe, U. O., Ukhurebor, K. E. & Muchiri, P. W. Facile synthesis and applications of carbon nanotubes in heavy metal remediation and biomedical fields: A comprehensive review. *J. Mol. Struct.* **1238**, 130462. <https://doi.org/10.1016/j.molstruc.2021.130462> (2021).
13. Ukhurebor, K. E. *et al.* Effect of hexavalent chromium on the environment and removal techniques: A review. *J. Environ. Managem.* **280**, 111809. <https://doi.org/10.1016/j.jenvman.2020.111809> (2021).
14. Mohanan, N., Montazer, Z., Sharma, P. & Levin, D. Microbial and enzymatic degradation of synthetic plastics. *Front. Microbiol.* **2020**, 11. <https://doi.org/10.3389/fmicb.2020.580709> (2020).
15. Hassaan, M. A., El Nemr, A. & Madkour, F. F. Testing the advanced oxidation processes on the degradation of direct blue 86 dye in wastewater. *Egypt. J. Aquat. Res.* **43**, 11–19. <https://doi.org/10.1016/j.ejar.2016.09.006> (2017).
16. Hassaan, M. A., El Nemr, A. & Madkour, F. F. Advanced oxidation processes of mordant Violet 40 dye in freshwater and seawater. *Egypt. J. Aquat. Res.* **43**, 1–9. <https://doi.org/10.1016/j.ejar.2016.09.004> (2017).
17. El-Nemr, A. *et al.* Advanced oxidation of AY-11 dye effluent: Detoxification and Degradat mechanism. *Toxin Rev.* **40**, 1472–1480. <https://doi.org/10.1080/15569543.2020.1736098> (2021).
18. Hassaan, M. A. & El NemrRagab, A. S. Green synthesis and application of metal and metal oxide nanoparticles. *Handb. Nanomater. Nanocomposit. Energy Env. Appl.* **36**, 831–857 (2021).
19. Hassaan, M. A., Elkatory, M. R. & El Nemr, A. Applications of photochemical oxidation in Textile Industry. *Handb. Nanomater. Nanocomposit. Energy Env. Appl.* **86**, 1975–2003 (2021).
20. El-Nemr, M. A., Abdelmonem, N. M., Ismail, I., Ragab, S. & El Nemr, A. Ozone and ammonium hydroxide modification of biocharprepared from Pisum sativum peels improves the adsorption of copper (II) from an aqueous medium. *Environ. Process.* **7**(3), 973–1007. <https://doi.org/10.1007/s40710-020-00455-2> (2020).
21. El-Nemr, M. A., Abdelmonem, N. M., Ismail, I., Ragab, S. & El Nemr, A. The efficient removal of the hazardous azo dye acid orange 7 from water using modified biochar from pea peels. *Desal. Wat. Treat.* **203**, 327–355. <https://doi.org/10.5004/dwt.2020.26190> (2020).
22. El-Nemr, M. A., Abdelmonem, N. M., Ismail, I., Ragab, S. & El Nemr, A. Removal of acid yellow 11 dye using novel modified biochar derived from watermelon peels. *Desal. Wat. Treat.* **203**, 403–431. <https://doi.org/10.5004/dwt.2020.26207> (2020).
23. El-Nemr, M. A., Abdelmonem, N. M., Ismail, I., Ragab, S. & El Nemr, A. Amination of biochar derived from watermelon peel by triethylenetetramine and ammonium hydroxide for toxic chromium removal enhancement. *Chin. J. Chem. Eng.* **36**, 199–222 (2021).
24. Sahlabji, T. *et al.* High surface area microporous activated carbon from pisum sativum peels for hexavalent chromium removal from aquatic environment. *Toxin Rev.* **41**(2), 639–649. <https://doi.org/10.1080/15569543.2021.1908361> (2022).
25. Aragaw, T. A. & Bogale, F. M. Biomass-based adsorbents for removal of dyes from wastewater: A review. *Front. Environ. Sci.* **9**, 1–24. <https://doi.org/10.3389/fenvs.2021.764958> (2021).
26. Aigbe, U. O. *et al.* A facile review on the sorption of heavy metals and dyes using bionanocomposites. *Adsorp. Sci. Tech.* **8030175**, 1–36. <https://doi.org/10.1155/2022/8030175> (2022).
27. Ayalew, A. A. & Aragaw, T. A. Utilization of treated coffee husk as low-cost bio-sorbent for adsorption of methylene blue. *Adsorp. Sci. Tech.* **38**, 205–222. <https://doi.org/10.1177/0263617420920516> (2020).
28. Khezrianjoo, S. & Revanasiddappa, H. D. photocatalytic degradation of acid yellow 36 using zinc oxide photocatalyst in aqueous media. *J. Cataf.* **2013**, 25 (2013).
29. Saha, A. & Pandit, P. Removal of Acid Yellow 36 and Rhodamine B from single and binary systems by reverse micelles. *Inte. J. Chem. Tech. Res.* **13**(4), 383–393 (2020).
30. Moradi, M., Ghanbari, F. & Minaee-Tabrizi, E. Removal of acid yellow 36 using Box-Behnken designed photoelectro-Fenton: A study on removal mechanisms. *Toxicol. Environ. Chem.* **97**(6), 700–709 (2015).
31. Thirunavukkarasu, A., Muthukumar, K. & Nithya, R. Adsorption of acid yellow 36 onto green nanoceria and amine functionalized green nanoceria: Comparative studies on kinetics, isotherm, thermodynamics, and diffusion analysis. *J. Taiwan Inst. Chem. Eng.* **93**, 211–225. <https://doi.org/10.1016/j.jtice.2018.07.006> (2018).
32. Wong, Y. C., Ranjini, K. N. & Wan-Nurdiyana, W. A. Removal of Congo red and acid yellow 36 dye using orange peel and rice husk as absorbent. *Orient. J. Chem.* **30**(2), 529 (2014).
33. Sheikh Mohammadi, A., Sardar, M., Mohammadi, A., Azimi, F. & Nurieh, N. Equilibrium and kinetic studies on the adsorption of acid yellow 36 dye by pinecone. *Arch. Hyg. Sci.* **2**(4), 158–164 (2013).
34. Sathya, M., Elumalai, S. & Muthuraman, G. Removal of Acid Yellow 36 from aqueous solution by solvent extraction method using tri-octyl amine as a carrier. *Int. J. Chem. Tech. Res.* **7**(7), 3014–3019 (2015).
35. Kashfiyalas, M., Khosravi, M., Marandi, R. & Seyyedi, K. Treatment of dye solution containing colored index acid yellow 36 by electrocoagulation using iron electrodes. *Int. J. Environ. Sci. Technol.* **2**(4), 365 (2006).
36. Xie, Y. *et al.* Ultra-high pyridinic N-doped porous carbon monolith enabling high-capacity K-ion battery anodes for both half-cell and full-cell applications. *Adv. Mater.* **29**(35), 1702268 (2017).
37. Inagaki, M., Toyoda, M., Soneda, Y. & Morishita, T. Nitrogen-doped carbon materials. *Carbon* **132**, 104–140 (2018).
38. Zou, K. *et al.* Hierarchically porous nitrogen-doped carbon derived from the activation of agriculture waste by potassium hydroxide and urea for high-performance supercapacitors. *J. Power Sourc.* **378**, 579–588 (2018).
39. Guo, D. *et al.* N-doped hierarchically micro-and mesoporous carbons with superior performance in supercapacitors. *Electrochim. Acta.* **291**, 103–113 (2018).
40. Chang, Y. *et al.* N, P-doped carbon material with suppressed water splitting activity for high-energy aqueous supercapacitors. *Carbon* **170**, 127–136 (2020).
41. Zhu, P., Li, X., Yao, H. & Pang, H. Hollow cobalt-iron prussian blue analogue nanocubes for high-performance supercapacitors. *J. Energy Stor.* **31**, 101544 (2020).
42. Yu, H. J. *et al.* Carbon nanosheets: Nitrogen-doped porous carbon nanosheets templated from g-C₃N₄ as metal-free electrocatalysts for efficient oxygen reduction reaction. *Adv. Mater.* **28**(25), 5080–5086 (2016).
43. Jin, W. *et al.* In-situ HDO of guaiacol over nitrogen-doped activated carbon supported nickel nanoparticles. *Appl. Catal. A Gener.* **620**, 118033 (2021).

44. Chen, J. *et al.* Outstanding supercapacitor performance of nitrogen-doped activated carbon derived from shaddock peel. *J. Energy Stor.* **39**, 102640 (2021).
45. Hsu, C. C. *et al.* Improved performance and long-term stability of activated carbon doped with nitrogen for capacitive deionization. *Desalination* **481**, 114362 (2020).
46. Dai, P. *et al.* Cotton fabrics-derived flexible nitrogen-doped activate d carbon cloth for high-performance supercapacitors in organic electrolyte. *Electrochim. Acta* **354**, 136717 (2020).
47. Dong, D. *et al.* High performance aqueous supercapacitor based on nitrogen-doped coal-based activated carbon electrode materials. *J. Coll. Inter. Sci.* **580**, 77–87 (2020).
48. Huang, Y., Li, J., Du, P. & Lu, X. Rational design of copper encapsulated within nitrogen-doped carbon core-shell nanosphere for efficiently photocatalytic peroxymonosulfate activation. *J. Coll. Inter. Sci.* **597**, 206–214 (2021).
49. Sun, Y. *et al.* Biomass-derived nitrogen self-doped porous activation carbon as an effective bifunctional electrocatalysts. *Chin. Chem. Lett.* **32**, 92–98 (2021).
50. Liu, Z., Du, Z., Xing, W. & Yan, Z. Facial synthesis of N-doped microporous carbon derived from urea furfural resin with high CO₂ capture capacity. *Mat. Lett.* **117**, 273–275 (2014).
51. Rouquerol, F., Rouquerol, J. & Sing, K. S. W. *Adsorption by Powders and Porous Solids* (Academic Press INC., 1999).
52. Gregg, S. J. & Sing, K. S. W. *Adsorption Surface Area and Porosity* 2nd edn. (Academic Press INC., 1982).
53. Stephen, B., Emmett, P. H. & Edward, T. Adsorption of gases in multimolecular layers. *J. Am. Chem. Soc.* **60**, 309 (1938).
54. Barrett, E. P., Joyner, L. G. & Halenda, P. P. The determination of pore volume and area distributions in porous substances. I. Computations from nitrogen isotherms. *J. Am. Chem. Soc.* **73**(1), 373–380 (1951).
55. Yilmaz, M. *et al.* The use of mandarin-biochar-O₃-TETA (MBT) produced from mandarin peels as a natural adsorbent for the removal of acid red 35 (AR35) dye from water. *Env. Proc.* **9**(3), 1–32. <https://doi.org/10.1007/s40710-022-00592-w> (2022).
56. Shoaib, A. G., El-Sikaily, A., El Nemr, A., Mohamed, A. E. D. A. & Hassan, A. A. Testing the carbonization condition for high surface area preparation of activated carbon followed Type IV from green alga *Ulva lactuca*. *Biomass Convers. Biorefin.* **12**, 3303–3318. <https://doi.org/10.1007/s13399-020-00823-w> (2022).
57. Shoaib, A. G., El-Sikaily, A., El Nemr, A., Mohamed, A. E. D. A. & Hassan, A. A. Preparation and characterization of highly surface area activated carbons followed Type IV from marine red alga (*Pterocladia capillacea*) by zinc chloride activation. *Biomass Convers. Biorefin.* **12**, 2253–2265. <https://doi.org/10.1007/s13399-020-00760-8> (2022).
58. El-Nemr, M. A. *et al.* Microporous activated carbon from *Pisum sativum* pods using various activation methods and tested for adsorption of acid orange 7 dye from water. *Molecules* **27**, 4840. <https://doi.org/10.3390/molecules27154840> (2022).
59. Liu, Y. L., Cheng, H. & He, Y. T. Application and mechanism of sludge-based ctivated carbon for phenol and cyanide removal from bio-treated effluent of coking wastewater. *Processes* **8**(1), 82. <https://doi.org/10.3390/pr8010082> (2020).
60. Kim, N. D., Buchholz, D. B., Casillas, G., José-Yacamán, M. & Chang, R. P. Hierarchical design for fabricating cost-effective high performance supercapacitors. *Adv. Funct. Mater.* **24**, 4186–4194 (2014).
61. Glenis, S., Nelson, A. & Labes, M. Sulfur doped graphite prepared via arc discharge of carbon rods in the presence of thiophenes. *J. Appl. Phys.* **86**, 4464–4466 (1999).
62. Chen, H. *et al.* Nitrogen and sulfur self-doped activated carbon directly derived from elm flower for high-performance supercapacitors. *ACS Omega* **3**(4), 4724–4732 (2018).
63. Xing, Z. *et al.* One-pot hydrothermal synthesis of Nitrogen-doped graphene as high-performance anode materials for lithium ion batteries. *Sci. Rep.* **6**(1), 1–10 (2016).
64. Yang, R. *et al.* The excellent performance of nitrogen-doped porous carbon nanowires modified activated carbon as air cathode catalyst for microbial fuel cells. *J. Solid State Electrochem.* **23**(12), 3437–3447. <https://doi.org/10.1007/s10008-019-04403-5> (2019).
65. Yao, Y., Bing, H., Feifei, X. & Xiaofeng, C. Equilibrium and kinetic studies of methyl orange adsorption on multi walled carbon nanotubes. *Chem. Eng. J.* **170**, 82–89 (2011).
66. Jalil, A. A. *et al.* Adsorption of methyl orange from aqueous solution onto calcined Lapindo volcanic mud. *J. Hazard. Mater.* **181**, 755–762 (2010).
67. Chen, S. *et al.* Equilibrium and kinetic studies of methyl orange and methyl violet adsorption on activated carbon derived from *Phragmites australis*. *Desalination* **252**, 149–156 (2010).
68. Han, Y. *et al.* Sorption of methylene blue by carboxy methyl cellulose and reuse process in a secondary sorption. *Coll. Surf. A* **380**, 143–151 (2011).
69. Wenxuan, Z. *et al.* Adsorption of anionic dyes from aqueous solutions using chemically modified straw. *Bio. Resour. Technol.* **117**, 40–47 (2012).
70. Albarelli, J. Q., Rabelo, R. B., Santos, D. T., Beppu, M. M. & Meireles, M. A. A. Effects of supercritical carbon dioxide on waste banana peels for heavy metal removal. *J. Supercrit. Fluids* **58**(3), 343–351 (2011).
71. Dönmez, G. C., Aksu, Z. & Özturk, A. A comparative study on heavy metal biosorption characteristics of some algae. *Process. Biochem.* **34**, 885–892 (1999).
72. Nuhoglu, Y., Malkoc, E., Gürses, A. & Canpolat, N. The removal of Cu(II) from aqueous solutions by *Ulothrix zonata*. *Bioresour. Technol.* **85**, 331–333 (2005).
73. Limousin, G. *et al.* Sorption isotherms: A review on physical bases, modeling and measurement. *Appl. Geochem.* **22**, 249–275 (2007).
74. Allen, S. J., Mckay, G. & Porter, J. F. Adsorption isotherm models for basic dye adsorption by peat in single and binary component systems. *J. Coll. Inter. Sci.* **280**, 322–333 (2004).
75. Kumar, K. V. & Sivanesan, S. Sorption isotherm for safranin onto rice husk: Comparison of linear and non-linear methods. *Dyes Pigm.* **72**, 130–133 (2007).
76. Ghiaci, M., Abbaspur, A., Kia, R. & Seyedeyn-Azad, F. Equilibrium isotherm studies for the sorption of benzene, toluene, and phenol onto organo-zeolites and as-synthesized MCM-41. *Sep. Purif. Technol.* **40**, 217–229 (2004).
77. Ncibi, M. C. Applicability of some statistical tools to predict optimum adsorption isotherm after linear and non-linear regression analysis. *J. Haz. Mater.* **153**, 207–212 (2008).
78. El Nemr, A., El-Sikaily, A. & Khaled, A. Modeling of adsorption isotherms of Methylene Blue onto rice husk activated carbon. *Egypt. J. Aquat. Res.* **36**, 403–425 (2010).
79. Malek, A. & Farooq, S. Comparison of isotherm models for hydrocarbon adsorption on activated carbon. *AIChE J.* **42**(11), 3191–3201 (1996).
80. Langmuir, I. The constitution and fundamental properties of solids and liquids. *J. Am. Chem. Soc.* **38**(11), 2221–2295 (1916).
81. Boer, J. H. *Dynamical Character of Adsorption* 2nd edn. (Oxford University Press, 1968).
82. Myers, A. L. & Prausnitz, J. M. Thermodynamics of mixed-gas adsorption. *AIChE J.* **11**(1), 121–127 (1965).
83. Dubinin, M. M. The potential theory of adsorption of gases and vapors for adsorbents with energetically non-uniform surface. *Chem. Rev.* **60**, 235–266 (1960).
84. Doğan, M., Alkan, M. & Onganer, Y. Adsorption of methylene blue from aqueous solution onto perlite. *Wat. Air Soil Pollut.* **120**, 229–249 (2000).
85. Freundlich, H. M. F. Über die adsorption in lösungen. *Zeitschr. Phys. Chem. (Leipzig)* **57A**, 385–470 (1906).
86. Tempkin, M. J. & Pyzhev, V. Recent modifications to Langmuir isotherms. *Acta Physiochim. URSS* **12**, 217–222 (1940).

87. Kavitha, D. & Namasivayam, C. Experimental and kinetic studies on methylene blue adsorption by coir pith carbon. *Bio. Technol.* **98**, 14–21 (2007).
88. Radushkevich, L. V. Potential theory of sorption and structure of carbons. *Zh. Fiz. Khim.* **23**, 1410–1420 (1949).
89. Dubinin, M. M. Modern state of the theory of volume filling of micropore adsorbents during adsorption of gases and steams on carbon adsorbents. *Zh. Fiz. Khim.* **39**, 1305 (1965).
90. Dubinin, M. M. & Radushkevich, L. V. The equation of the characteristic curve of activated charcoal. *Proc. Acad. Sci. Phys. Chem. Sect. USSR* **55**, 331–333 (1947).
91. Halsey, G. D. Physical adsorption in nonuniform surfaces. *J. Chem. Phys.* **16**, 931–945 (1948).
92. Rosen, M. J. *Surfactants and Interfacial Phenomena*, 32–76 (Wiley, 1978).
93. Kumar, K. V. Comparative analysis of linear and non-linear method of estimating the sorption isotherm parameters for malachite green onto activated carbon. *J. Hazard. Mater.* **B136**, 197–202 (2006).
94. Lataye, D. H., Mishra, I. M. & Mall, I. D. Adsorption of 2-picoline onto bagasse fly ash from aqueous solution. *Chem. Eng. J.* **138**(1–3), 35–46 (2008).
95. Boulinguez, B., Le Cloirec, P. & Wolbert, D. Revisiting the determination of Langmuir parameters application to tetrahydrothiophene adsorption onto activated carbon. *Langmuir* **24**, 6420–6424 (2008).
96. Kumar, K. V., Porkodi, K. & Rocha, F. Isotherms and thermodynamics by linear and non-linear regression analysis for the sorption of methylene blue onto activated carbon: Comparison of various error functions. *J. Hazard. Mater.* **151**, 794–804 (2008).
97. Kumar, K. V. & Sivanesan, S. Pseudo second order kinetics and pseudo isotherms for malachite green onto activated carbon: Comparison of linear and nonlinear regression methods. *J. Hazard. Mater.* **B136**, 721–726 (2006).
98. Mane, V. S., Mall, I. D. & Srivastava, V. C. Kinetic and equilibrium isotherm studies for the adsorptive removal of Brilliant Green dye from aqueous solution by rice husk ash. *J. Env. Manag.* **84**(4), 390–400 (2007).
99. Ng, J. C. Y., Cheung, W. H. & McKay, G. Equilibrium studies of the sorption of Cu (II) ions onto chitosan. *J. Coll. Int. Sci.* **255**(1), 64–74 (2002).
100. Kapoor, A. & Yang, R. T. Correlation of equilibrium adsorption data of condensable vapours on porous adsorbents. *Gas Sep. Purif.* **3**, 187–192 (1989).
101. Ng, J. C. Y., Cheung, W. H. & McKay, G. Equilibrium studies for the sorption of lead from effluents using chitosan. *Chemosphere* **52**(6), 1021–1030 (2003).
102. Marquardt, D. W. An algorithm for least-squares estimation of nonlinear parameters. *J. Soc. Ind. Appl. Math.* **11**, 431–441 (1963).
103. Wong, Y. C., Szeto, Y. S., Cheung, W. & McKay, G. Adsorption of acid dyes on chitosan-equilibrium isotherm analyses. *Process Biochem.* **39**(6), 695–704 (2004).
104. Mall, I. D., Srivastava, V. C., Agarwal, N. K. & Mishra, I. M. Adsorptive removal of malachite green dye from aqueous solution by bagasse fly ash and activated carbon-kinetic study and equilibrium isotherm analyses. *Colloids Surf. A Physicochem. Eng.* **264**(1–3), 17–28 (2005).
105. Mall, I. D., Srivastava, V. C., Agarwal, N. K. & Mishra, I. M. Removal of Congo red from aqueous solution by bagasse fly ash and activated carbon: Kinetic study and equilibrium isotherm analyses. *Chemosphere* **61**, 492–501 (2005).
106. Seidel, A. & Gelbin, D. On applying the ideal adsorbed solution theory to multicomponent adsorption equilibria of dissolved organic components on activated carbon. *Chem. Eng. Sci.* **43**, 79–89 (1988).
107. Ho, Y. S., Chiu, W. T. & Wang, C. C. Regression analysis for the sorption isotherms of basic dyes on sugarcane dust. *Bio. Tech.* **96**, 1285–1291 (2005).
108. Ho, Y. S., McKay, G., Wase, D. A. J. & Foster, C. F. Study of the sorption of divalent metal ions on to peat. *Adsorp. Sci. Technol.* **18**, 639–650 (2000).
109. Zeldowitsch, J. Über den mechanismus der katalytischen oxidation von CO and MnO₂. *Acta Physicochim. URSS* **1**, 364–449 (1934).
110. Chien, S. H. & Clayton, W. R. Application of Elovich equation to the kinetics of phosphate release and sorption on soils. *Sci. Soc. Am. J.* **44**, 265–268 (1980).
111. Sparks, D. L. *Kinetics of Reactions in Pure and in Mixed Systems* 83–145 (Soil physical chemistry, 1986).
112. Weber, W. J. & Morris, J. C. Kinetics of adsorption on carbon from solution. *J. Sanit. Eng. Div. Am. Soc. Civ. Eng.* **89**, 31–60 (1963).
113. Srinivasan, K., Balasubramanian, N. & Ramakrishan, T. V. Studies on chromium removal by rice husk carbon. *Indian J. Environ. Health* **30**, 376–387 (1988).
114. Boyd, G. E., Adamson, A. M. & Myers, L. S. The exchange adsorption of ions from aqueous solution by organic zeolites. *J. Am. Chem. Soc.* **69**, 2836 (1949).
115. Tan, K. L. & Hameed, B. H. Insight into the adsorption kinetics models for the removal of contaminants from aqueous solutions. *J. Taiwan Inst. Chem. Eng.* **74**, 25–48 (2017).
116. Tan, H. N., You, S. J., Hosseini-Bandegharai, A. & Chao, H. P. Mistakes and inconsistencies regarding adsorption of contaminants from aqueous solutions: A critical review. *Water Res.* **120**, 88–116 (2017).
117. Ho, Y. S. & McKay, G. The kinetics of sorption of basic dyes from aqueous solution by sphagnum moss peat. *Can. J. Chem. Eng.* **76**, 822–827 (1998).
118. Dotto, G. L. & Pinto, L. A. A. Adsorption of food dyes onto chitosan: Optimization process and kinetic. *Carbohydr. Polym.* **84**(1), 231–238 (2011).
119. Cheung, C. W., Porter, J. F. & McKay, G. Elovich equation and modified secondorder equation for sorption of cadmium ions onto bone char. *J. Chem. Technol. Biotechnol.* **75**(11), 963–970 (2000).
120. Cheung, C. W., Porter, J. F. & McKay, G. Adsorption kinetic analysis for the removal of cadmium ions from effluents using bone char. *Water Res.* **35**, 605–612 (2001).
121. Kargi, F. & Cikla, S. Biosorption of zinc (II) ions onto powdered waste sludge (PWS): Kinetics and isotherms. *Enzyme Microb. Technol.* **38**, 705–710 (2006).
122. Hamdaoui, O. Batch study of liquid-phase adsorption of methylene blue using cedar sawdust and crushed brick. *J. Hazard. Mater.* **B135**, 264–273 (2006).
123. Annadurai, G., Juang, R. S. & Lee, D. J. Use of cellulose-based wastes for adsorption of dyes from aqueous solutions. *J. Hazard. Mater.* **92**(3), 263–274 (2002).
124. Boyd, G. E., Adamson, A. W. & Myers-Jr, L. S. The exchange adsorption of ions from aqueous solutions by organic zeolites. II. Kinetics. *J. Am. Chem. Soc.* **69**(11), 2836–2848 (1947).
125. Patel, Y. N. & Patel, M. P. Adsorption of azo dyes from water by new poly (3-acrylamidopropyl)-trimethylammonium chloride-co-N, N-dimethylacrylamide superabsorbent hydrogel—equilibrium and kinetic studies. *J. Environ. Chem. Eng.* **1**(4), 1368–1374 (2013).
126. Garg, D., Kumar, S., Sharma, K. & Majumder, C. B. Application of waste peanut shells to form activated carbon and its utilization for the removal of Acid Yellow 36 from wastewater. *Groundw. Sustain. Dev.* **8**, 512–519 (2019).
127. Wijetunga, S. & Gunasekara, C. D. F. A. Evaluation of refused tea waste activated carbon for color removal: Equilibrium and kinetic studies. *Adv. Environ. Res.* **6**(1), 1–14 (2017).
128. Mahmoodi, N. M., Hayati, B. & Arami, M. Isotherm and kinetic studies of dye removal from colored textile wastewater using date seed. *JCST.* **5**(4), 325–333 (2011).

Author contributions

The practical portion was led by Eng. M.A.E., who also wrote the manuscript and submitted to the journal. Dr. M.A.H. oversaw the analyses work. The work was supervised by Professor I.A.

Funding

Open access funding provided by The Science, Technology & Innovation Funding Authority (STDF) in cooperation with The Egyptian Knowledge Bank (EKB). This work was partially supported by The Science, Technology & Innovation Funding Authority (STDF) of Egypt, project number SCSE-31235.

Competing interests

The authors declare no competing interests.

Additional information

Supplementary Information The online version contains supplementary material available at <https://doi.org/10.1038/s41598-023-33075-5>.

Correspondence and requests for materials should be addressed to M.A.E.-N.

Reprints and permissions information is available at www.nature.com/reprints.

Publisher's note Springer Nature remains neutral with regard to jurisdictional claims in published maps and institutional affiliations.



Open Access This article is licensed under a Creative Commons Attribution 4.0 International License, which permits use, sharing, adaptation, distribution and reproduction in any medium or format, as long as you give appropriate credit to the original author(s) and the source, provide a link to the Creative Commons licence, and indicate if changes were made. The images or other third party material in this article are included in the article's Creative Commons licence, unless indicated otherwise in a credit line to the material. If material is not included in the article's Creative Commons licence and your intended use is not permitted by statutory regulation or exceeds the permitted use, you will need to obtain permission directly from the copyright holder. To view a copy of this licence, visit <http://creativecommons.org/licenses/by/4.0/>.

© The Author(s) 2023